Master Thesis

Noise Investigation on the LISA Pathfinder Optical Bench Ground Setup

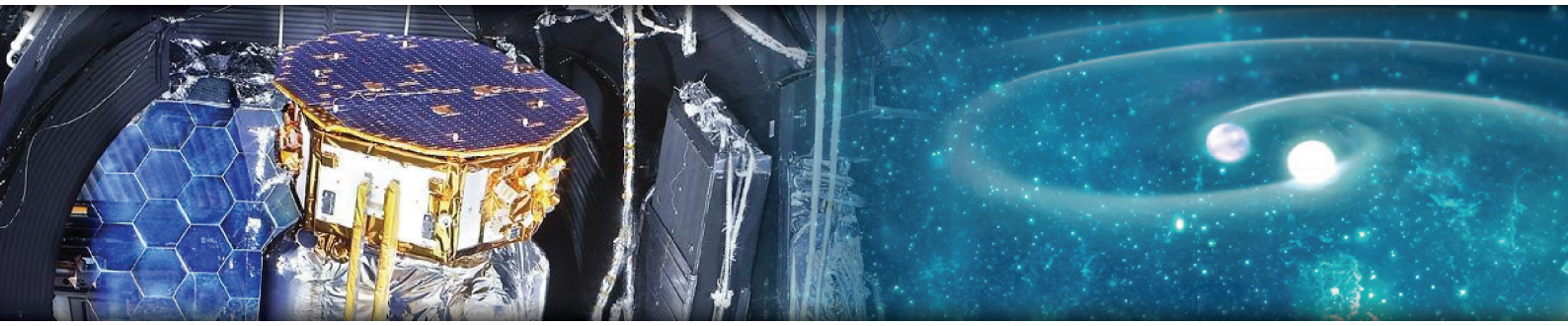

by Andreas Wittchen

Master Thesis

Noise Investigation on the LISA-Pathfinder Optical Bench Ground Setup

by
Andreas Wittchen

born at
21nd August 1988 in Braunschweig

November 12, 2013

Leibniz Universität Hannover
Institut für Gravitationsphysik der Universität Hannover
Albert-Einstein-Institut Hannover
Max-Planck-Institut für Gravitationsphysik

First Examiner: Prof. Dr. Karsten Danzmann

Second Examiner: PD Dr. Gerhard Heinzel

Abstract

The subject of this thesis is noise investigations on the LISA Pathfinder OMS ground setup. LISA Pathfinder (LPF) is a planned ESA technology demonstration space-mission, the LPF spacecraft features an optical measurement system similar to the LISA mission. LISA is a planned triangular laser telescope with a million kilometres arm length on an orbit around the sun. Distance fluctuations between two free falling test masses per arm are measured with heterodyne interferometry.
The LPF flight model features two test masses about 0.38 m apart. Test mass motion on earth is realised with piezoelectric actuators. During this thesis the noise dependence on different test mass positions was investigated. The test masses of the flight model (FM) are placed in a housing in the spacecraft, the implications of which on the interferometer performance were simulated with a housing mockup.

Abstract

Diese Arbeit beschäftigt sich mit der Untersuchung von Rauschen des LISA Pathfinder OMS Boden Aufbaus. LISA Pathfinder (LPF) ist eine geplante ESA technologie demonstrations Weltraummission, der LPF Satellit ist mit einem optischen Messsystem ähnlich dem der LISA Mission ausgestattet. Bei LISA handelt es sich um ein geplantes Laser Teleskop in dreiecksform mit einer Million Kilometer Armlänge, dieses Teleskop befindet sich in einem Orbit um die Sonne. Änderungen der Entfernung zwischen zwei frei fallenden Testmassen pro Arm werden mit Heterodyne Interferometrie gemessen.
Das LPF FM ist ebenfalls mit zwei Testmassen ausgestattet, diese sind 0.38 m voneinander entfernt. Auf der Erde werden die Testmassen mit piezoelektrischen Aktoren bewegt. In dieser Arbeit wird die Beziehung zwischen Testmassenposition und Rauschlevel untersucht. Die Testmassen des FM befinden sich in einem Gehäuse im Satelliten, der Einfluss von diesem Gehäuse auf das Interferometer wird mit einem Mockup simuliert.

Contents

List of Figures

Acronyms

AEI Albert-Einstein-Institute

AO Analysis Object

BS Beam Splitter

GUI General User Interface

GW Gravitational Wave

LISA Laser Interferometer Space Antenna

LSD Linear Spectral Density

LTPDA LISA Technology Package Data Analysis

LO Local Oszillator

LPF LISA Pathfinder

MB Modulation Bench

OB Optical Bench

OMS Optical Metrology System

OPD Optical Path Length Difference

PD Photo Diode

PM Phasemeter

QPD Quadrant Photodiode

TM Test Mass

TM1 Test Mass 1

TM2 Test Mass 2

X1 Measurement Interferometer for Displacement of TM1 relativ to the OB

X12 Measurement Interferometer for Relative Displacement between TM1 and TM2

XF Frequency Interferometer

XR Reference Interferometer

1 Introduction

Albert Einstein published his Theory of General Relativity in 1915. A relationship between space-time curvature and gravitation was postulated, the cause of the space-time curvature is mass and energy. Motion of masses produces changes of the curvature; it is postulated that these travel at the speed of light. Accelerated masses lead to oscillations of space-time, which we call gravitational waves [1].
Theory predicts only weak interaction with other physical phenomena, which makes them difficult to detect. However, this has the advantage that GWs provide undisturbed information on distant sources. These objects might be binary systems of black holes or neutron stars, both of which constitute high mass and high density.
Russell A. Hulse and Joseph H. Taylor, Jr, both of Princeton University, were awarded with the Nobel Prize in Physics in 1993 for their indirect measurement of gravitational waves. The orbital period of the binary pulsar $PSR1913+16$ was measured over several years. The extremely stable pulse period of the pulsar is used as reference. A decline in the orbit period of 75 ms per year was measured and attributed to a loss of energy through gravitational waves[2].
Currently space is only observed through the electromagnetic spectrum. A telescope for gravitational waves will provide a new outlook into space. To this end a laser interferometric space antenna (LISA) is planned, a triangular interferometer with a million kilometre arm length. Distance fluctuations by gravitational waves between two free falling test masses per arm are measured with picometer precision, this enables the measurement of space-time distortions.
Since this space telescope is an ambitious project the technology demonstration mission LISA Pathfinder (LPF) is planned. The LPF engineering model ground setup is in Hannover at the AEI and will be the subject of this thesis.
In LPF instead of a million kilometres the distance between the free falling test masses is only 38 cm, longitudinal and angular motion of the test masses are measured by heterodyne interferometry with quadrant photodiodes. Instead of real test masses the ground setup features mirrors, where motion is generated with piezoelectric actuators [3].
Two modulated laser beams are interfered on a recombination beam splitter. The measurement beam is reflected on the test masses, motion is measured via interference with the reference beam.
Noise suppression is achieved with five control loops. For each beam power fluctuations are measured and suppressed with the amplitude control loop. The fre-

quency interferometer measures frequency noise. A separate control loop for fast and longterm frequency fluctuations is implemented. With the reference interferometer phase noise arising from various environmental disturbances is measured. Phase noise between the two beams is suppressed with the optical path length difference loop; with a piezoelectric actuator the optical path length is changed.
Remaining amplitude and phase noise is suppressed by subtracting the reference interferometer signal from the other signals. Theoretical predictions show that the efficiency of this subtraction depends on the phase difference between reference signal and the other signals. Measurements of this effect are part of this thesis.
In the flight model the test masses are placed in a housing, and the measurement beam travels through a hole in this housing on the way to the test mass. So far this housing was not implemented in the ground setup. During the course of this thesis a mockup of the housing was designed and implemented. Measurements to determine the influence of the housing on the beam path are performed [4] [5] [6] [7].

2 The ground setup

On the LISA Pathfinder satellite the free fall of two test masses at the first Lagrangian point between the earth and sun will be monitored. The position and orientation of both need to be measured with picometer and microradian accuracy, respectively.
Two heterodyne laser interferometers are placed between the test masses, one measures the distance fluctuations between test mass one and the satellite, the other between test mass one and two. Quadrant photodiodes are used for all interferometers, allowing the calculation of the test mass angular motion through differential wavefront sensing (DWS).

Various noise sources disturb the accurate measurements, but careful design and construction of this optical metrology system minimizes many of them. The interferometers, for example, are bonded on an optical bench made of zerodur, a material which is very thermally stable. For other noise sources active control loops are implemented. In this thesis the laser frequency and amplitude control loops, and the optical path length difference control loop will be briefly discussed.
Amplitude fluctuations are measured with two additional single element photodiodes. Two more interferometers are bonded on the zerodur optical bench for frequency and optical path length difference control.

On the ground the setup is similar, however mirrors are used instead of test masses. They are mounted on piezoelectric actuators to allow us to simulate test mass movement (see Chapter 3). Two frequency shifted laser beams for heterodyne interferometry are provided by the modulation bench (MB)(see Chapter 2.2) and are fed into a vacuum tank to the optical bench (OB) via optical fibres (see Chapter 2.1).
Similar to the flight model, four interferometers are bonded on the optical bench. The X_1 interferometer measures the distance fluctuations between test mass mirror one (TM1) and the centre of the OB. The measurement beam hits TM1 on the way to the recombination beam splitter, where it is interfered with the reference beam. The measurement of the distance fluctuations between TM1 and TM2 is done by the X_{12} interferometer. The measurement beam is reflected on both test masses and is then interfered with the reference beam. The other two interferometers are responsible for noise suppression (see Chapter2.3). The frequency interferometer, X_F, measures frequency noise and is used in the frequency control loop to suppress

laser frequency fluctuations (see Chapter 2.3.3).
Common mode path length fluctuations as measured by X_R are subtracted in post processing (see Chapter 2.1 and Chapter 3.3). Path length changes between the two beams are suppressed with the optical path length difference loop (OPD loop)(see Chapter 2.3.2).
Interferometry signals from 8 quadrant photodiodes and laser power signals from two single element photodiodes are sent to a phasemeter and converted to digital signals and saved as time series. The LISA technology package data analysis (LTPDA toolbox) for MATLAB© is used for analysis (part of the code is described in Chapter 3.2).

2.1. The optical bench

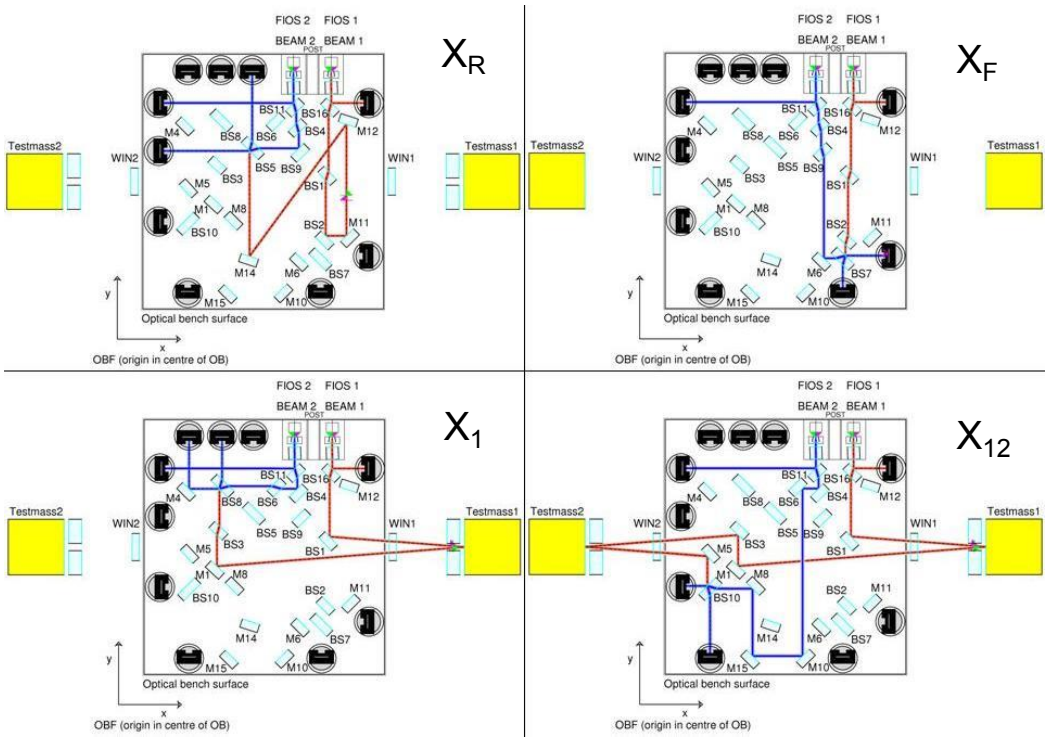

Figure 2.1.: This is the LISA Pathfinder optical bench engineering model. The measurement beam (red) is interfered with the reference beam (blue). The motion of two test masses (yellow) is measured by the X_1 interferometer (bottom left) and the X_{12} interferometer (bottom right). On the top right the frequency interferometer X_F is shown, the reference interferometer can be seen on the top left. The optical fibres have different length, the frequency interferometer has a total path length difference of 38 cm, the other three interferometers have no path length difference.

The EM optical bench (OB) is one key component of the optical metrology system (see Figure 2.1). It was designed at the AEI in Hannover and constructed at the Rutherford Appelton Laboratories with support from the AEI and the University of Glasgow. All components are bonded on the zerodur ground plate. Unlike glue,

bonding forms atomic bonds which leads to high stability.

As mentioned in the introduction four heterodyne Mach-Zehnder interferometers are placed on the optical bench. Two modulated beams with a frequency difference of f_{het} are sent from the modulation bench to the optical bench. The heterodyne interferometry will be explained in Chapter 2.1.1.

On the ground free fall is simulated with mirrors mounted on piezoelectric actuators, which allow longitudinal and angular motion. To avoid confusion these two specific mirrors will be called test mass mirrors, TM mirrors or TM1 and TM2.

The interferometer used to measure motion of TM1 relative to the optical bench is named X_1. The measurement beam and reference beam have the same optical path length when the TM mirror is in its nominal position. The beam hitting the TM is called the measurement beam; it is interfered at a recombination beam splitter with the reference beam (see Figure 2.1). The two outputs of the beam splitter are measured on quadrant photodiodes(QPD). The use of QPDs allow us to measure the relative angle between the beams, using a method called Differential Wavefront Sensing (DWS) (see Chapter 2.1.2).

Movement from the zero position leads to a path length change of the measurement beam, thus giving a phase difference between the two beams. This phase difference leads to a heterodyne signal, which is recorded by the phasemeter. With this information the phase difference is calculated in post-processing. It is important to note that only phase changes relative to the phase from the beginning of the measurement can be measured. On the ground the TM mirrors are positioned by hand; the position in the optical measurement system coordinate frame is not well known. In flight the absolute position is known via capacitive sensing to nm precision.

With a procedure similar to the X_1 interferometer the relative movement of TM2 to TM1 is measured with the X_{12} interferometer. The motion of TM2 is known via $X_{12} = X_1 - X_2$.

To suppress any phase changes not generated from motion of the test masses, two more interferometers are bonded on the optical bench. Like the measurement interferometers the reference interferometer X_R has no path length difference.

To account for instabilities of the laser, a frequency interferometer was built, where an intentional arm length difference of 38 cm allows a measurement of frequency noise (see Figure 2.1).

Amplitude fluctuations are measured with one single element photo diode per beam.

These components are best explained in context in the chapter about control loops (2.3).

The subject of this investigation is the engineering model (EM) of the optical bench. After the investigations by Felipe Guzmán Cervantes[4] the flight model was modified to avoid beam clipping. The functionality is the same, and all investigations on the engineering model are applicable for the flight model. [8][9][6] [10]

2.1.1. Heterodyne interferometry

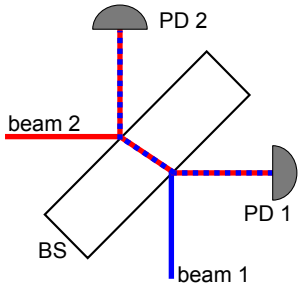

Figure 2.2.: A recombination beam splitter interferes two laser beams (red and blue), the interferometric signal is measured by photodiodes (PD).

For the following chapters a basic understanding of heterodyne interferometry is necessary. This subsection focuses on the interference of two frequency shifted linear polarized beams by a 50/50 non-polarizing recombination beam splitter.
The incoming beams can be described as

$$\begin{aligned} \vec{E_{\mathrm{r}}}(\vec{\mathrm{r}},t) &= E_{\mathrm{r}_0}(t)\vec{e_x}e^{-i(\vec{k}\vec{r}-2\pi f_{\mathrm{r}}t-\psi_{\mathrm{r}})} &&=: E_{\mathrm{r}}\vec{e_x}, \\ \vec{E_{\mathrm{m}}}(\vec{r},t) &= E_{\mathrm{m}_0}(t)\vec{e_y}e^{-i(\vec{k}\vec{r}-2\pi f_{\mathrm{m}}t-\psi_{\mathrm{m}}(t))} &&=: E_{\mathrm{m}}\vec{e_y}. \end{aligned}$$

TM motion is the reason for the time dependence of the measurement beam phase $\psi_{\mathrm{m}}(t)$, this is the main science output. The starting difference of the two phases is arbitrary and depends on TM positioning. For now only the phase change is of interest. The two beams have are modulated at two frequencies f_{m} and f_{r} with:

$$f_{\mathrm{het}} \;=\; f_{\mathrm{m}} - f_{\mathrm{r}}.$$

The transmission coefficient, τ, and reflective coefficient, ρ, of the recombination BS relate to the amplitude of the electric field. Conservation of energy yields

$$\tau^2 + \rho^2 \;=\; 1,$$

since the power of the beams is proportional to the square of their amplitude. Any losses are negligible. Beams reflected on a surface with a higher optical density receive a phase jump of π. The real value of the reflection coefficient, ρ, and the complex value of the transmission coefficient, $i\tau$, guarantee this phase jump and conservation of energy. For a 50/50 beam splitter it is known that

$$\tau \;=\; \rho \;=\; \frac{1}{\sqrt{2}}.$$

Using matrix optics a beam splitter (BS) can be described as follows

$$\begin{pmatrix} O_x(t) \\ O_y(t) \end{pmatrix} \;=\; \begin{pmatrix} i\tau & \rho \\ \rho & i\tau \end{pmatrix} \vec{E_{\mathrm{r}}}(\vec{\mathrm{r}},t) \cdot \vec{E_{\mathrm{m}}}(\vec{\mathrm{r}},t) \;=\; \begin{pmatrix} i\tau & \rho \\ \rho & i\tau \end{pmatrix} \begin{pmatrix} E_{\mathrm{r}} \\ E_{\mathrm{m}} \end{pmatrix}.$$

Interference of the reduced amplitude of the incoming beams leads to the outgoing beams $O_x(t)$ and $O_y(t)$,

$$\begin{pmatrix} O_x(t) \\ O_y(t) \end{pmatrix} = \begin{pmatrix} O_{\mathrm{symm}}(t) \\ O_{\mathrm{asymm}}(t) \end{pmatrix} = \begin{pmatrix} i\tau E_{\mathrm{r}} + \rho E_{\mathrm{m}}(t) \\ \rho E_{\mathrm{r}} + i\tau E_{\mathrm{m}}(t) \end{pmatrix}.$$

The current of the photo diode is proportional to the square of the incoming light amplitude measured on the symmetric output:

$$\begin{aligned} I_{\mathrm{symm}}(t) &\propto |i\tau E_{\mathrm{r}} + \rho E_{\mathrm{m}}(t)|^2, \\ &\propto (i\tau E_{\mathrm{r}} + \rho E_{\mathrm{m}}(t))\,(i\tau E_{\mathrm{r}} + \rho E_{\mathrm{m}}(t))^*, \\ &\propto \tau^2 E_{\mathrm{r}}^2 + \rho^2 E_{\mathrm{m}}^2 + i\tau\rho(E_{\mathrm{m}} E_{\mathrm{r}}^* + E_{\mathrm{r}} E_{\mathrm{m}}^*), \\ &\propto \tau^2 E_{\mathrm{r}}^2 + \rho^2 E_{\mathrm{m}}^2 + 2\tau\rho E_{\mathrm{m}} E_r \sin(2\pi_{\mathrm{het}} t - \psi_{\mathrm{m}}(t) - \psi_{\mathrm{r}}). \end{aligned}$$

The asymmetric port is phase shifted by π and yields:

$$I_{\mathrm{asymm}}(t) \propto \tau^2 E_{\mathrm{r}}^2 + \rho^2 E_{\mathrm{m}}^2 - 2\tau\rho, E_{\mathrm{m}} E_{\mathrm{r}} \sin(f_{\mathrm{het}} - \psi_{\mathrm{m}}(t) - \psi_{\mathrm{r}}).$$

$I_{\mathrm{symm}}(t)$ and $I_{\mathrm{asymm}}(t)$ are called heterodyne signals. From the photodiode these signals are sent to the phasemeter. The frequency difference f_{het} of the two beams gives the periodicity of the heterodyne signal; the phase is given by the path length difference of the two beam paths, and is given by

$$\begin{aligned} 2\tau\rho E_{\mathrm{m}} E_{\mathrm{r}} \sin(2\pi f_{\mathrm{het}} t - \psi_{\mathrm{m}}(t) - \psi_{\mathrm{r}}) &= a E_{\mathrm{m}} E_{\mathrm{r}} \sin(2\pi f_{\mathrm{het}} t - \Delta\psi(t)), \\ \Delta\psi(t) = \psi_{\mathrm{m}}(t) - \psi_{\mathrm{r}} &= \frac{2\pi\Delta L}{\lambda} = \frac{2\pi(L_{\mathrm{m}}(t) - L_{\mathrm{r}})}{\lambda}, \end{aligned}$$

where $\lambda = 1064\,\mathrm{nm}$ is the wavelength of the laser, $\Delta\psi(t)$ the measured phase difference change, and $L_{\mathrm{m}}(t)$ and L_{r} the optical path length of the measurement beam and reference beam, respectively. Variation of the path length $L_{\mathrm{m}}(t)$ leads to variations of $\Delta\psi(t)$. The data stream of the phasemeter contains the phase difference $\Delta\psi(t)$ as a time series, where, by definition, $\Delta\psi(0) = 0$.[8][11]

2.1.2. DWS measurement

The angular jitter of the test mass is important information during flight since the attitude couples into the longitudinal measurement. The orientation of the reflective surface of the test mass is measured by quadrant photodiodes, allowing us to subtract the cross-coupling in post processing.

As indicated by the name, the QPD consists of four photodiodes (see Figure 2.3), each of them measures a phase ψ_X depending on the phase difference between the measurement and reference beam on quadrant X. If the beams are not parallel when they reach the diode the quadrants will measure different phases. [4] [8] With this

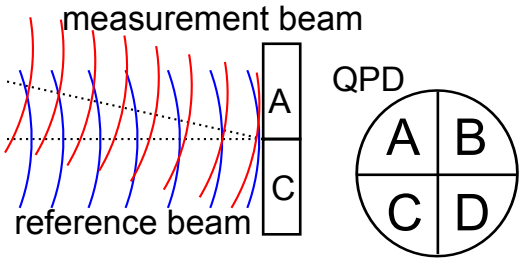

Figure 2.3.: Differential wavefront sensing. The measured phase on the four quadrants A, B, C, D differs depending on the angle between the two beams. Using this phase difference the angle between the incoming beams can be calculated.

information the angle between the two beams, and therefore the test mass angle, can be calculated:

$$\begin{aligned} \phi^{\mathrm{DWS}} &= \kappa^{\mathrm{DWS}}[(\psi_{\mathrm{A}}+\psi_{\mathrm{C}})-(\psi_{\mathrm{B}}+\psi_{\mathrm{D}})] \\ \nu^{\mathrm{DWS}} &= \kappa^{\mathrm{DWS}}[(\psi_{\mathrm{A}}+\psi_{\mathrm{B}})-(\psi_{\mathrm{C}}+\psi_{\mathrm{D}})] \end{aligned}$$

with the calibration factor $\kappa^{\mathrm{DWS}} \approx \frac{d}{\lambda} = 1.9 \cdot 10^3 \frac{\mathrm{rad}}{\mathrm{rad}}$ of DWS measurement to real test mass angle. This factor is dependant on the beam diameter $d \approx 2\,\mathrm{mm}$ at the photodiode and laser wavelength $\lambda = 1064\,\mathrm{nm}$.

The center of the reference beam is carefully aligned to the centre of the QPD, if the centre of the measurement beam moves on the QPD the power on the quadrants is different. [4] [11] Quadrants with a lower beam power have worse signal to noise ratio, but this approach gives the same weight to all quadrants. The signal on quadrant X can be expressed with the beam amplitude a_X,

$$\zeta_{\mathrm{X}} = a_{\mathrm{X}} e^{i\psi_{\mathrm{X}}}.$$

With this the test mass angle relative to the optical bench can be calculated with

$$\begin{aligned} \phi^{DWS} &= \kappa^{DWS} \arg\left(\frac{\zeta_{\mathrm{A}}+\zeta_{\mathrm{C}}}{\zeta_{\mathrm{B}}+\zeta_{\mathrm{D}}}\right), \\ \nu^{DWS} &= \kappa^{DWS} \arg\left(\frac{\zeta_{\mathrm{A}}+\zeta_{\mathrm{B}}}{\zeta_{\mathrm{C}}+\zeta_{\mathrm{D}}}\right). \end{aligned}$$

2.2. The modulation bench

On the modulation bench the output of a single laser is split into two beams called the measurement and reference beam. The laser is a Mephisto 500 with a wavelength of 1064 nm, the laser current is set to achieve a beam power of 400 mW. After a polarisation filter, a faraday isolator and one fibre, 150 mW arrive at the modulation bench.
A 50-50 beam splitter divides the beam; then both travel through acousto-optic modulators (AOM). The beam paths can be seen in Figure 2.4.
Bragg diffraction due to an acoustic wave propagating through a crystal is used to modulate the beam amplitude, since the refractive index of the crystal depends on the amplitude of the sound wave (see Figure 2.5).
Since light is scattered on gradients of the refractive index, a change of beam properties can be achieved. Light scattered from consecutive wavefronts is interfered constructively if

$$n\lambda_{\text{Laser}} = \Lambda_{\text{AOM}}(\sin\theta_{\text{in}} + \sin\theta_{\text{out}}),$$

where λ_{Laser} is the laser frequency and λ_{AOM} the frequency of the acoustic wave. θ_{in} and θ_{out} are the angles of the incoming and outgoing beam, respectively. The integer n denotes the order of diffraction. [12]

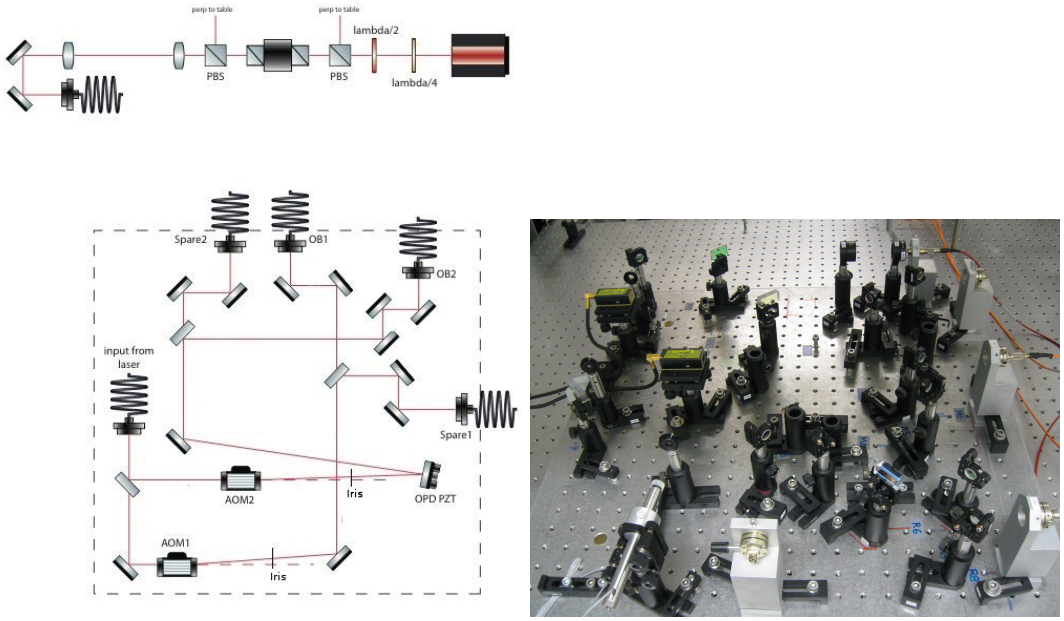

(a) Design **(b)** Photograph

Figure 2.4.: Design: The laser in the top right corner produces the beam. It is sent to the main part of the modulation bench via optical fibre. A beam splitter divides the beam into measurement and reference beam, which are amplitude modulated to produce sidebands by AOMs. Again optical fibres are used to send the two beams into a vacuum tank to the optical bench. The laser can not be seen on the photograph

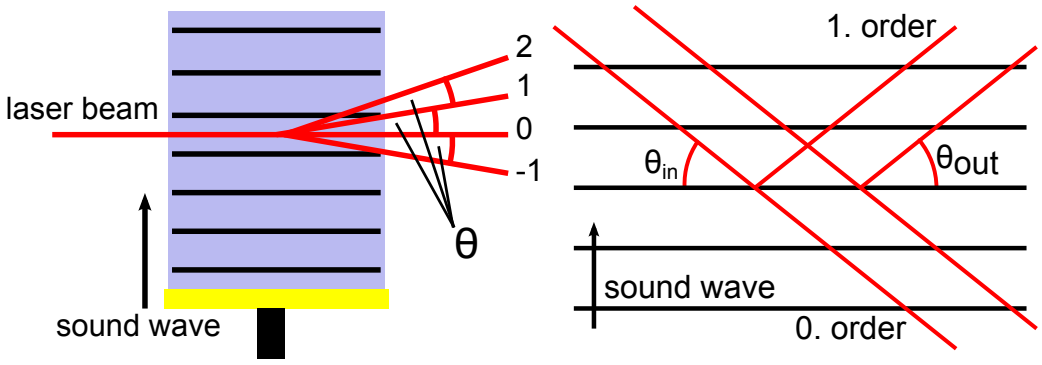

(a) AOM **(b)** Bragg diffraction

Figure 2.5.: On the left a simplified picture of an AOM is shown, the laser beam (red) travels through the crystal from the left, its path is affected by the acoustic wave (black). Constructive interference leads to multiple outgoing beams with different frequencies. On the right a simplified graphic of bragg diffraction is shown, the cause for the diffraction is a lattice structure. Here the structure consists of acoustic waves; more common examples are a crystal lattice or a fine comb.

In our setup the laser hits the crystal orthogonal to the crystal surface, therefore $\theta_{\text{in}} \approx 0$.
The Bragg diffraction due to an acoustic wave differs from the diffraction on an atomic lattice, where phonons cause the scattering of the photons. The first order was scattered by one phonon with the wavelength of the acoustic wave Θ_{AOM}, the second order by two phonons and so forth. The phonon is destroyed in the process, negative orders of diffraction can be thought of as the creation of phonons. If conservation of energy and momentum are considered it is obvious that the frequency from the amplitude modulation changes depending on the order of diffraction:

$$f_{\text{out}} = f_{\text{Laser}} + m\frac{\Lambda_{\text{AOM}}}{c}.$$

The lab AOMs are designed and adjusted to let a high amount of power into the first order (see Figure 2.5). An aperture is used to block the other orders. Theoretical descriptions of heterodyne interferometry describe the frequencies of the interfering beams as $f = f_{\text{Laser}} \pm \frac{f_{\text{het}}}{2}$. The diffraction in negative orders is not very efficient, additionally the desired heterodyne frequency is in the kHz range whereas the operation frequency of the AOMs is in the range of MHz. This leads to the final frequencies

$$\begin{aligned} f_{\text{meas}} &= f_{\text{Laser}} + f_{\text{AOM}} + \tfrac{f_{\text{het}}}{2}, \\ f_{\text{ref}} &= f_{\text{Laser}} + f_{\text{AOM}} - \tfrac{f_{\text{het}}}{2}. \end{aligned}$$

Both are first order beams. The LPF laser frequency is $f_{\text{Laser}} = \frac{1064\,\text{nm}}{c} = 282\,\text{THz}$. The heterodyne frequency in this setup is $f_{\text{het}} = 1623.37\,\text{Hz}$, the AOMs have a nominal frequency of $f_{\text{AOM}} = 80\,\text{MHz}$.[13]

Both beams are then coupled into optical fibres and fed into the vacuum tank and to the optical bench. In front of the fibres the beams have a power of 20mW; around 4mW arrive on the optical bench. Routine alignment is necessary to maintain these power levels.

2.3. Control loops

Reaching the required picometer precision is a challenging task. Control elements are needed to suppress various noise sources. The optical bench is bonded on a thermally stable zerodur baseplate, additionally the whole setup is placed in a vacuum tank. Even so, long term temperature fluctuations are still visible in the measurements. However, these are out of the measurement band.
The tank is not shielded from ground vibrations, these can lead to jitter of the TM mirrors. The best measurements were done through the night or over the weekend. The noise suppression methods through control loops will be explained in the following subsections; the three loops were already mentioned in Chapter 2.1, and an overview is given by Figure 2.6.

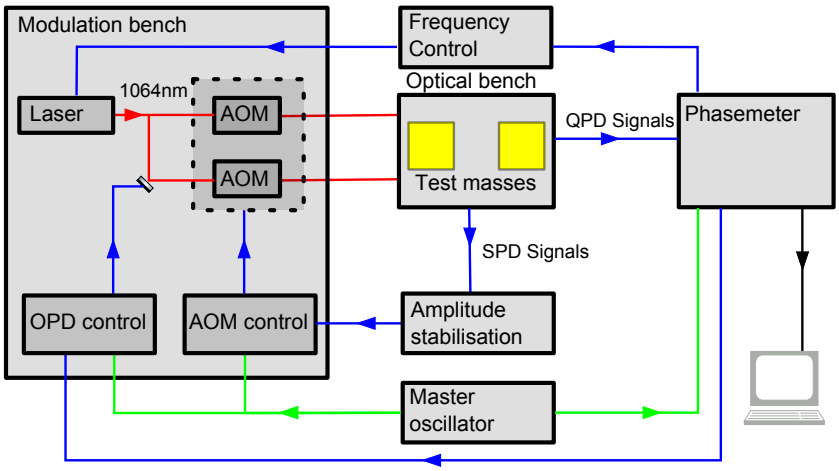

Figure 2.6.: This is the full OMS Ground Setup. From the modulation bench the beam is sent to the interferometers on the optical bench, the Signals from the Photodiodes are send to the phasemeter. The control loops shown in this setup are explained in the text. In the ground setup the test masses (yellow) are piezo actuated mirrors.

2.3.1. Amplitude noise

In Chapter 2.1.1 the laser power on the photodiode was derived. The amplitudes E_1 and E_2 of the beams were assumed to be stable, but a wide frequency range of amplitude noise is a property of the laser beam:

$$E = E(t) = E + \delta E(t).$$

With this, the formula for the heterodyne signal can be written as:

$$I_{\mathrm{het}} = aE_{\mathrm{m}}(t)E_{\mathrm{r}}(t)\sin(1\pi f_{\mathrm{het}}t - \Delta\psi(t)).$$

Amplitude noise with a the heterodyne frequency, f_{het}, couples into the length measurement. To measure the amplitude noise two single element photodiodes are placed on the optical bench behind a beam splitter, directly after the fibre output couplers. Electric current corresponding to $E_1(t)^2$ or $E_2(t)^2$ is sent to a control circuit, called the amplitude box.

The photodiode current output $I(t) = I_{\mathrm{DC}} + \delta I$ is converted to a voltage $U(t)$. A DC voltage offset is subtracted, which leaves the small variations, δU. These are then amplified and fed back to the AOMs to change the amplitude of the acoustic wave, thus changing the beam power of the first diffraction order.[13][14][15]

Plots of performance measurements with and without the amplitude loop can be seen in Figure 2.7.

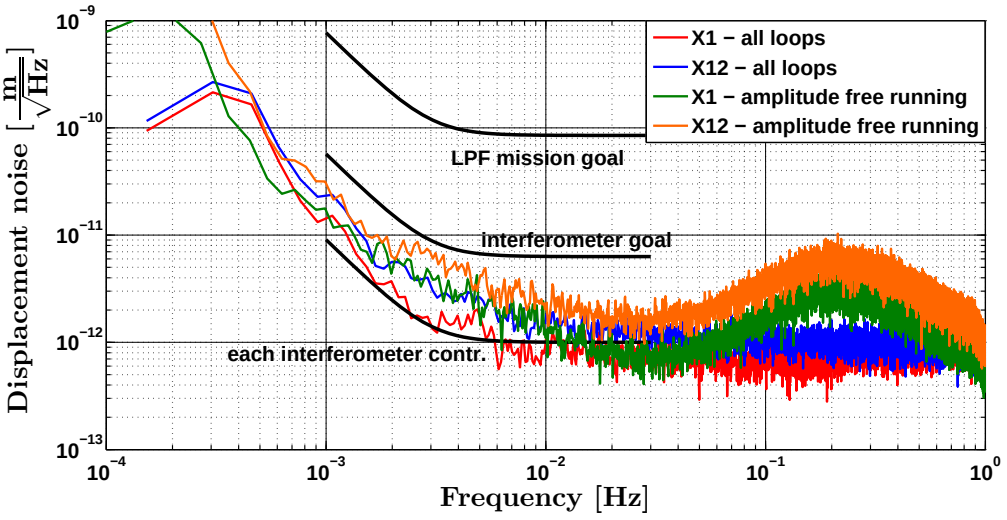

Figure 2.7.: The noise level of the ground setup is measured with all loops active (red and blue), and then without the amplitude loop (green and orange). The black curves show the noise performance goals.

2.3.2. Phase noise

Any phase changes consist of the following contributions

$$\Delta\phi = \delta\phi_{\mathrm{TM}} + \delta\phi_{\mathrm{OB}} + \delta\phi_{\mathrm{common}} + \delta\phi_{\mathrm{differential}}.$$

The phase ϕ_{TM} is only on the measurement beam of the measurement interferometers X_1 and X_12, caused by motion of the test mass mirrors. This is the main science output. Any path length changes arising from deformation of the optical bench $\delta\phi_{\mathrm{OB}}$ are negligible in this discussion since they're out of the measurement band.
The reference interferometer has no arm length difference and is fully built on the optical bench, any phase changes measured are due to environmental fluctuations. These phase changes are considered as noise and are present in the measurement interferometers as well. The signal from the reference interferometer is taken and fed to a piezo actuated mirror on the modulation bench in the path of the reference beam. If phase changes between the reference and measurement beams are measured the mirror is moved in the opposite direction to adjust the optical path length. This control loop is called the optical path length difference loop, or OPD loop for short (see Figure 2.9).[13] [16]
This OPD loop only suppresses path length difference noise between the measurement and reference beams. Any phase changes present in both beams (common mode phase noise), can't be suppressed. The effect on the measurement interferometers can be seen in Figure 2.8.
Since X_R, X_1 and X_{12} have the same macroscopic path length difference between measurement and reference beam this common mode noise can be mostly subtracted. [5]
In the LTPDA processing chain the phase information in radians is used to calculate test mass movement in meters; the corresponding method is called `omsCalibrateLong`. In this step the reference interferometer phase is subtracted from the other phase information:

$$\begin{aligned}
\Phi_{\mathrm{R}}[\mathrm{m}] &= \frac{4\pi}{\lambda}\phi_{\mathrm{R}}[\mathrm{rad}] \\
\Phi_{\mathrm{X1}}[\mathrm{m}] &= \frac{4\pi}{\lambda}(\phi_{\mathrm{X1}}[\mathrm{rad}] - \phi_{\mathrm{R}}[\mathrm{rad}]), \\
\Phi_{\mathrm{X12}}[\mathrm{m}] &= \frac{4\pi}{\lambda}(\phi_{\mathrm{X12}}[\mathrm{rad}] - \phi_{\mathrm{R}}[\mathrm{rad}]), \\
\Phi_{\mathrm{XF}}[\mathrm{m}] &= \frac{4\pi}{\lambda}(\phi_{\mathrm{XF}}[\mathrm{rad}] - \phi_{\mathrm{R}}[\mathrm{rad}]).
\end{aligned}$$

The efficiency of this subtraction depends on the microscopic phase difference between the reference and measurement signal.
The amplitude loop treats both beams separately; it doesn't make a difference if the amplitude noise is common mode or not. Any remaining amplitude noise present in all four interferometers is subtracted in this step as well; efficiency of this subtraction also depends on the microscopic phase difference.

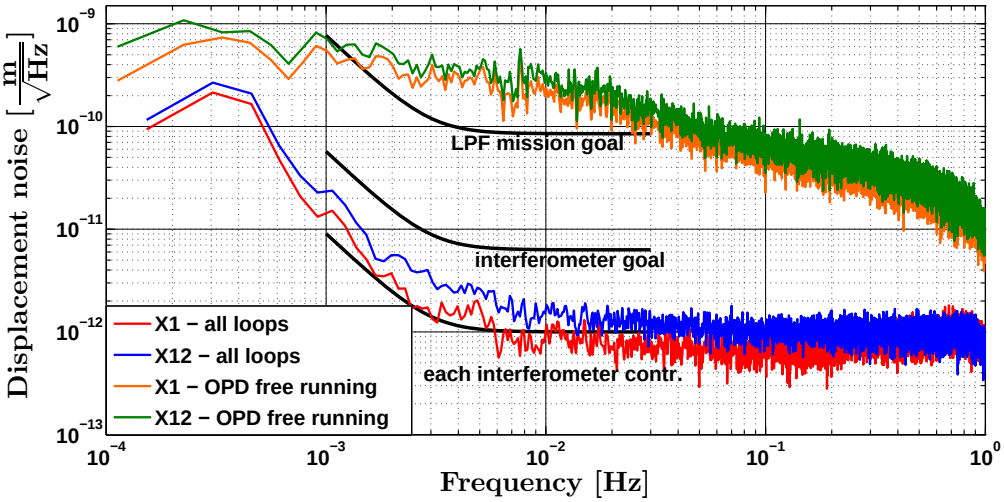

Figure 2.8.: The noise level is measured with (red+blue) and without (orange+green) the OPD loop. Without the phase noise stabilisation the performance is more than two orders of magnitude worse, the noise level in the measurement band is above the LPF mission goal.

These effects are described in detail in Chapter 3.[17][18]

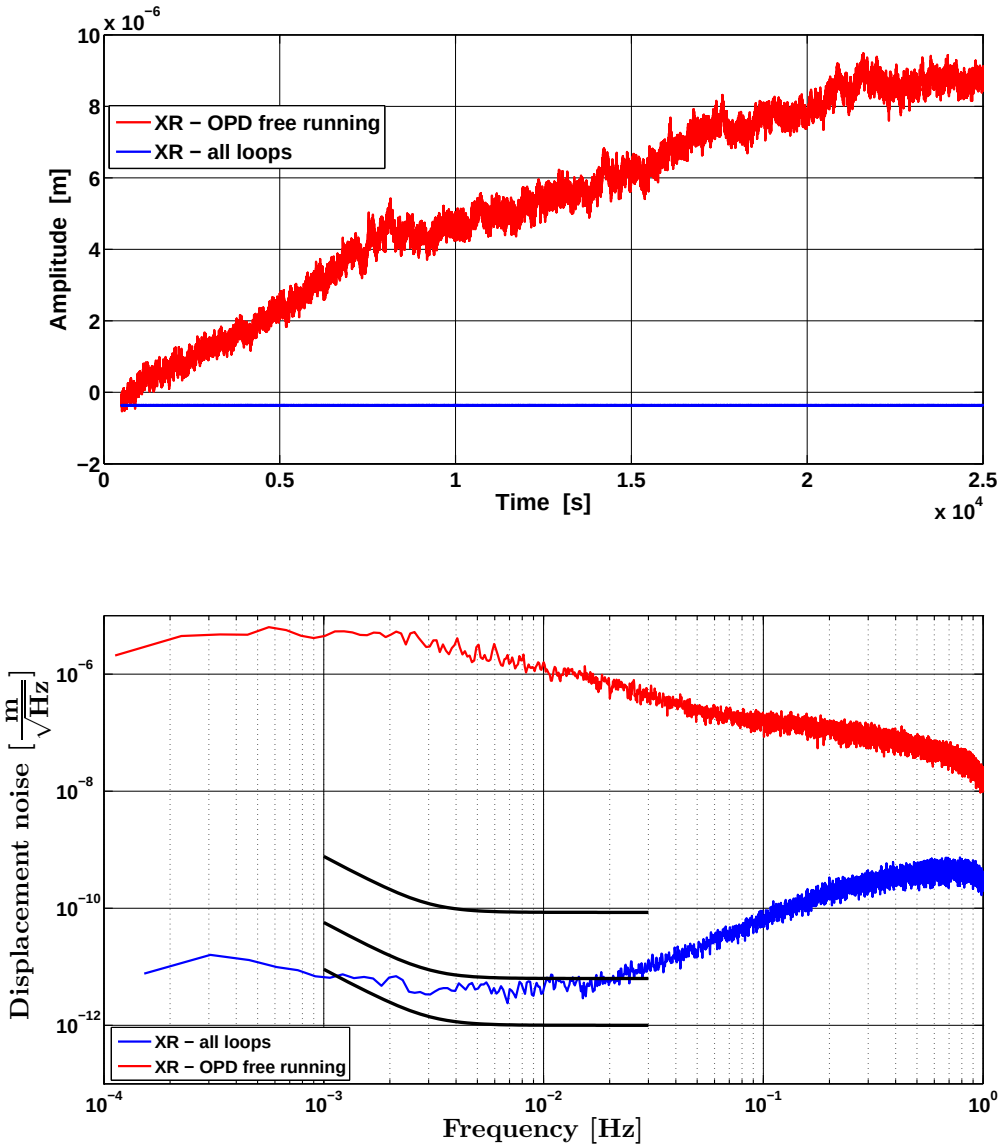

Figure 2.9.: The top picture shows a time series of the reference interferometer output. The measured displacement in meters is plotted over time, the measured motion without the OPD loop (red) is caused by path length noise between the two beams. With the OPD loop these are suppressed (blue).
The second plot shows the amplitude spectral density of these two measurements.

2.3.3. Frequency noise

Laser frequency noise transfers to phase noise if there is a path length difference between the two beams, by

$$\delta x = \frac{\delta\nu}{\nu}\delta L,$$

where δx is the apparent path length fluctuation, $\delta\nu$ is the laser frequency noise and δL is the path length difference.
The X_R, X_1 and X_{12} interferometers were designed to have no path length difference. The actual path length difference in the flight model is affected by alignment and mechanical tolerances, and the frequency stability requirements were calculated with a worst-case value of 1 cm.

An additional interferometer with an intentionally large path length difference of 38 cm between measurement and reference beam is used to measure the frequency fluctuations. Similar to the other interferometers the reference interferometer signal is subtracted from the frequency interferometer signal. The laser `Mephisto 500` from `Innolight` has two inputs to change the frequency. Fast frequency changes can be achieved with a piezo which puts strain on the laser crystal, the frequency can be changed with a response bandwidth of 100 kHz and a range of 0.1 GHz. Slower frequency adjustments with a range of over 30 GHz can be achieved by adjustment of the laser crystal temperature. The response bandwidth is limited to fractions of a Herz. Laser frequency fluctuations with a frequency lower than 1.6 kHz are sent to the temperature input. This is the slow frequency control loop. The fast frequency control loop sends frequency fluctuations with a frequency higher than 1.6 kHz to the piezo input on the laser head. [13] [5][15]
The effect of the frequency control loop on the performance of the measurement interferometers can be seen in Figure 2.10, the effect on the X_F output can be seen in Figure 2.11.

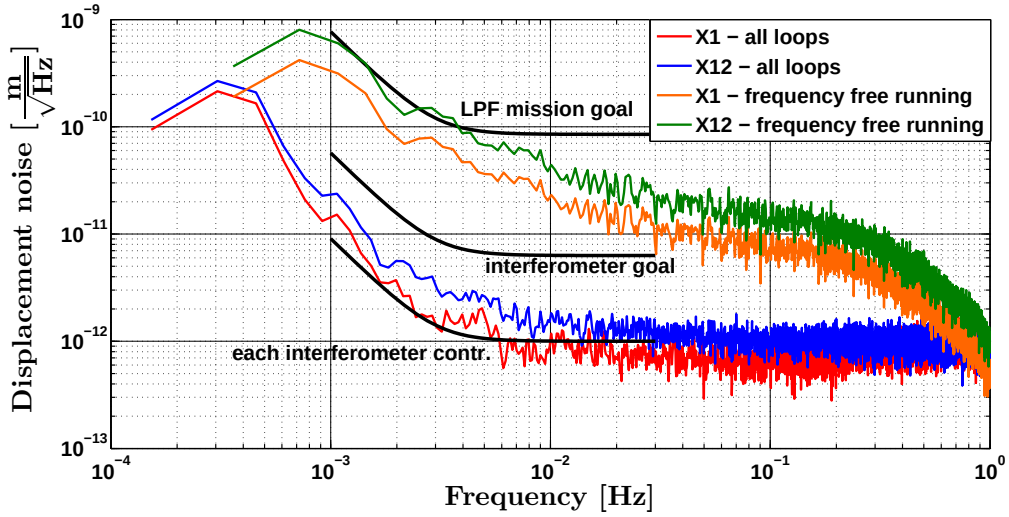

Figure 2.10.: The noise level is measured with (red+blue) and without (orange+green) frequency loop. Without the laser stabilisation the performance is more than one order of magnitude worse.

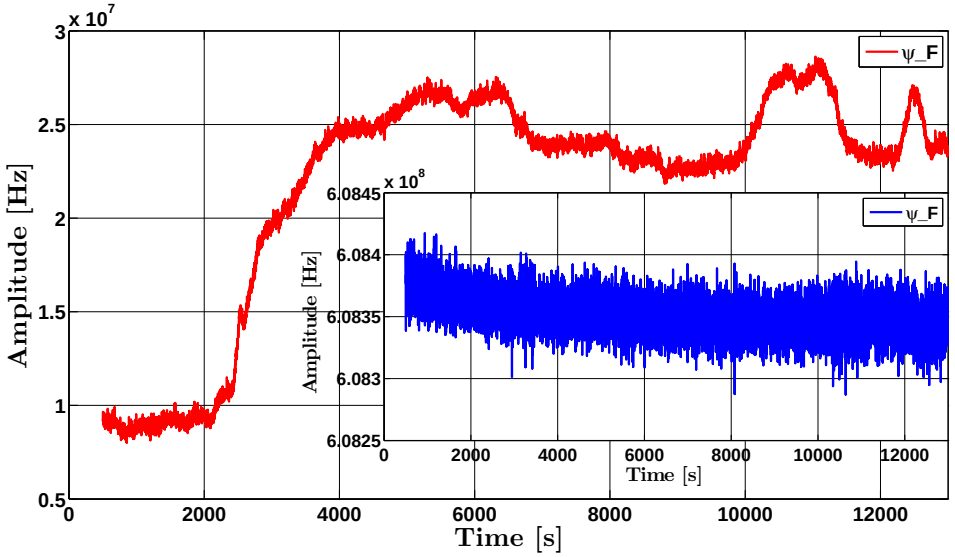

Figure 2.11.: In red the frequency interferometer output without laser frequency stabilisation is shown, the blue curve shows a similar plot with frequency control. As seen in Figure 2.10 the displacement noise with loops is one order of magnitude smaller.

3 Test mass motion

In the previous chapter environmental fluctuations were the only cause for test mass motion. A more controlled movement with a bigger range of motion can be achieved with piezoelectric actuators. The test mass mirrors are mounted on the piezo, and motion is generated either with a function generator or a DC voltage supply to generate continuous motion as well as step functions. This setup is described briefly in Chapter 3.1. The displacement noise of the measurement interferometers depends on the phase difference between the measurement and reference beams. Calculation of an average noise level over time and phase difference is done in MATLAB©; the method is described in Chapter 3.2. This effect is investigated in Chapter 3.3. These investigations provide experimental demonstration of the theoretical discussions in the recent paper 'Common mode noise rejection properties of amplitude and phase noise in a heterodyne interferometer'by Gerald Hechenblaikner from EADS Astrium (see Chapter 3.3). [18]

3.1. Experimental setup

To simulate the movement of the test mass the ground setup mirror is glued on to a piezoelectric actuator, which consists of three pieces. Each piece can be moved individually to generate longitudinal and angular motion (see Chapter 3.1.1).
The three piezos are operated from a driver circuit which has three inputs, one for longitudinal and two for angular motion (see Chapter 3.1.2). Measurements of the impact of the driver on the noise performance are shown in Chapter 3.1.3, effects of driver input on the noise performance will be shown in Chapter 3.4, together with intentional laser frequency drift as a method to create a phase difference between the two beams.

3.1.1. Piezoelectric actuator

The piezoeletric actuator consists of three individual pieces, each with its own input. The three pieces are placed in an equilateral triangle, with the pivot point in the middle. The pivot point is the centre point of rotation of any lever system, in this experiment a simple reflective surface. After proper calibration, angular motion of the reflective surface about the pivot point should not result in any longitudinal motion.

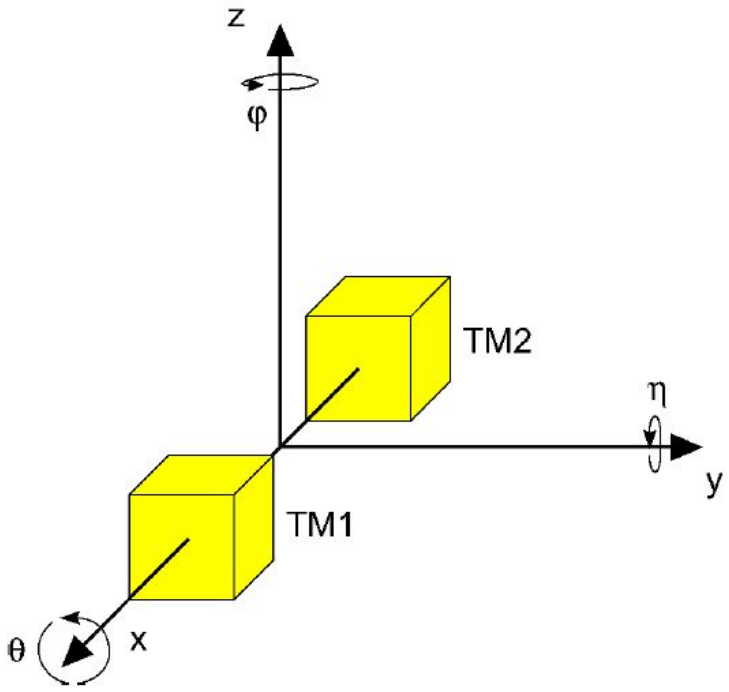

Figure 3.1.: This is the coordinate frame of the LPF optical metrology system.

For longitudinal movement, in the x direction, all three piezo parts have to be connected to a nominally equal voltage; for angular motion the input voltage is scaled differently. These voltages depend on the spatial relation between the individual piezo and the desired TM motion angle. The TM motion axes are defined with the optical bench as reference. The axis perpendicular to the optical bench surface is named z; η is the variable for angular motion around this axis. The variable for angular motion around the y-Axis is ϕ. Angular motion around the longitudinal axis, θ, can't be achieved with this device (see Figure 3.1).
The relation between motion in x, η and ϕ of the test mass and the input voltage into the three individual piezos Z, A and B can be expressed by

$$\begin{pmatrix} x \\ \phi \\ \eta \end{pmatrix} = \begin{pmatrix} l_1 & l_2 & l_3 \\ p_1 & p_2 & p_3 \\ e_1 & e_2 & e_3 \end{pmatrix} \begin{pmatrix} Z \\ A \\ B \end{pmatrix}.$$

In general a voltage is applied to all three inputs. The set of constants l_i have the unit $[\frac{\mathrm{m}}{\mathrm{V}}]$, the other sets p_i and e_i are in $[\frac{\mathrm{rad}}{\mathrm{V}}]$. The values of the latter two sets depend strongly on the orientation of the piezo.

3.1.2. Driver

An electronic driver circuit exists to drive the piezo. By design one input channel of the driver relates to one possible motion of the piezoelectric actuator. Input to inZ leads to longitudinal movement x, angular motion in ϕ and η can be achieved with inA and inB, respectively.

Each input channel leads to a voltage on all three driver outputs Z, A and B (see Figure 3.2). Another matrix to calculate these from a given input can be defined. Since for every movement of the test mass mirror all three piezos must be used, the transfer matrix of the driver has non-diagonal elements. Calibration of the driver should be done in a way that the resulting matrix is the inverse of the piezo matrix (see Chapter 3.1.1), multiplied with a scaling vector, such that

$$\begin{pmatrix} Z \\ A \\ B \end{pmatrix} = \begin{pmatrix} L_1 & L_2 & L_3 \\ P_1 & P_2 & P_3 \\ E_1 & E_2 & E_3 \end{pmatrix} \begin{pmatrix} inZ \\ inA \\ inB \end{pmatrix}.$$

In an ideal setup the matrix of the driver and of the piezo combine to a matrix consisting only of diagonal elements:

$$\begin{pmatrix} x \\ \phi \\ \eta \end{pmatrix} = \begin{pmatrix} l_1 & l_2 & l_3 \\ p_1 & p_2 & p_3 \\ e_1 & e_2 & e_3 \end{pmatrix} \begin{pmatrix} L_1 & L_2 & L_3 \\ P_1 & P_2 & P_3 \\ E_1 & E_2 & E_3 \end{pmatrix} \begin{pmatrix} inZ \\ inA \\ inB \end{pmatrix} = \begin{pmatrix} L & 0 & 0 \\ 0 & P & 0 \\ 0 & 0 & E \end{pmatrix} \begin{pmatrix} inZ \\ inA \\ inB \end{pmatrix}.$$

The first step to set up the system is to decouple the degrees of freedom.

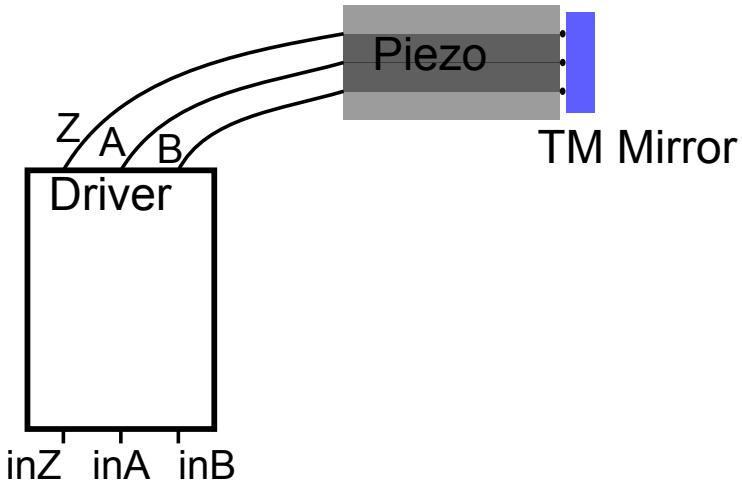

Figure 3.2.: Notation for input and output of the driver setup. Voltage input to inZ leads to longitudinal motion of the piezo; inA and inB lead to angular motion.

For the longitudinal direction the inZ input is used. A sine wave input (for example 1 Vpp, 1 Hz) is fed in, and the output is observed on an oscilloscope. Then the potentiometers P1 and P2 are adjusted until all three outputs are the same. The calibration of angular motion can only be done when the driver is connected to the piezo. Test mass motion can be seen in real-time on the phasemeter readout display.

To obtain the coupling coefficients, as well as the actual movement to a given input voltage, a function generator provides a sine signal. The signal can easily be seen in an amplitude spectrum, or directly in the time series if the signal is strong enough

(see Figures 3.3 and 3.4).

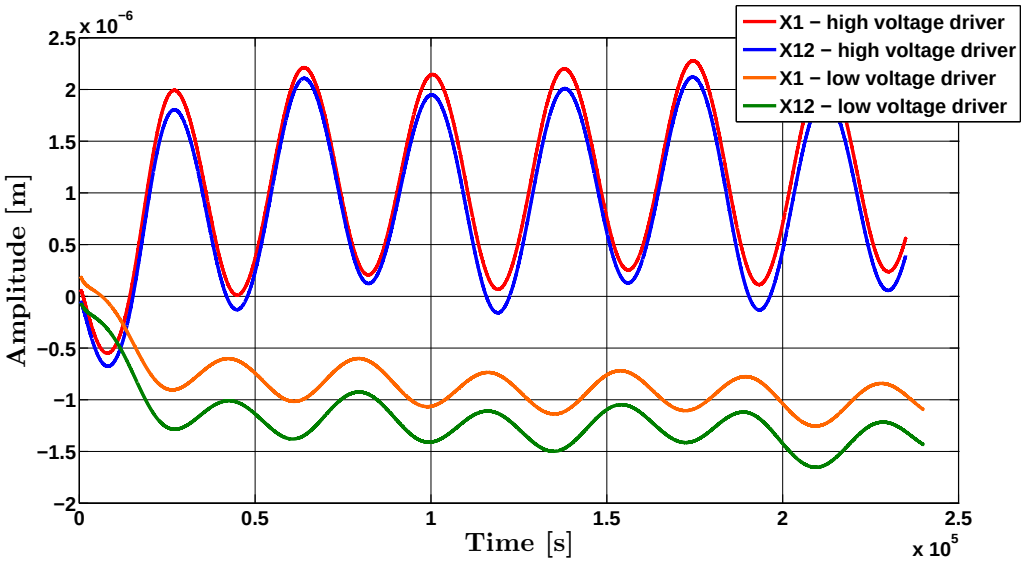

Figure 3.3.: Comparison of piezo range with high voltage driver input and low voltage input, both measurements were performed with 2 Vpp and 0.00027 Hz input from the function generator

The scaling constants L, P and E can be measured, and for smaller voltages the behaviour is linear. Multiple experiments are done where the only change in the setup is the chosen input channel. More than one channel can be used at a time if different frequencies are chosen.
The driver has three different output levels. One set of three for test and low voltage purposes, one set for high voltage output and bigger movements, and a monitor set. For the first two the transfer coefficients and changes in the noise level were measured (see Chapter 3.1.3). The coefficients change every time the piezo is physically moved or the driver potentiometers are adjusted. Measured coupling coefficients for a low voltage input (0.1 mHz) can be seen below, coefficients below or near the noise level are indicated with 0:

$$\begin{pmatrix} x \\ \phi \\ \eta \end{pmatrix} = \begin{pmatrix} 3.615\,\frac{\mathrm{nm}}{\mathrm{mV}} & 0.034\,\frac{\mathrm{nm}}{\mathrm{mV}} & 0.0015\,\frac{\mathrm{nm}}{\mathrm{mV}} \\ 0\,\frac{\mathrm{nrad}}{} & 698\,\frac{\mathrm{nrad}}{\mathrm{mV}} & 1.9\,\frac{\mathrm{nrad}}{\mathrm{mV}} \\ 0\,\frac{\mathrm{nrad}}{\mathrm{mV}} & 6.72\,\frac{\mathrm{nrad}}{\mathrm{mV}} & 127\,\frac{\mathrm{nrad}}{\mathrm{mV}} \end{pmatrix} \begin{pmatrix} inZ \\ inA \\ inB \end{pmatrix}.$$

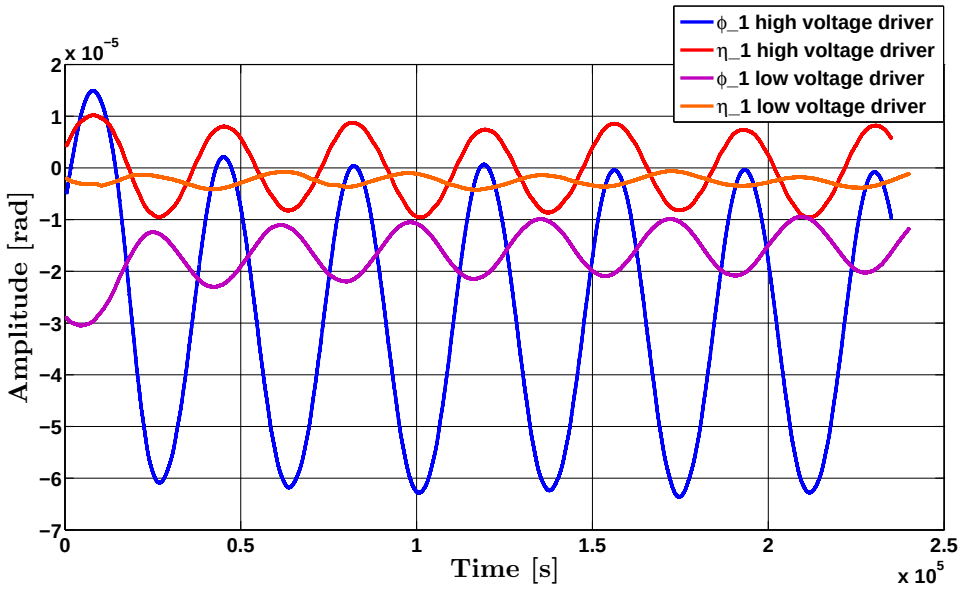

Figure 3.4.: Comparison of piezo range with high voltage driver input (around 2 μm) and low voltage input (less than 0.5 μm).

3.1.3. Noise performance

Measurements with different driver setups were performed. All control loops are turned on. When the high voltage output of the driver is used the noise level of the measurement interferometers rises one and a half orders of magnitude. The test output of the driver produces excess noise at higher frequencies, about one order of magnitude around 0.1 Hz. In the measurement band the noise level is comparable to a performance measurement without a driver after a month of continuous measurements (see Figures 3.5 and Figure 3.6).
If an experiment requires a good noise performance the high voltage output of the driver can not be used. Additionally the digitalisation of the function generator output has to be taken into account. This will be especially relevant in Chapter 3.4.

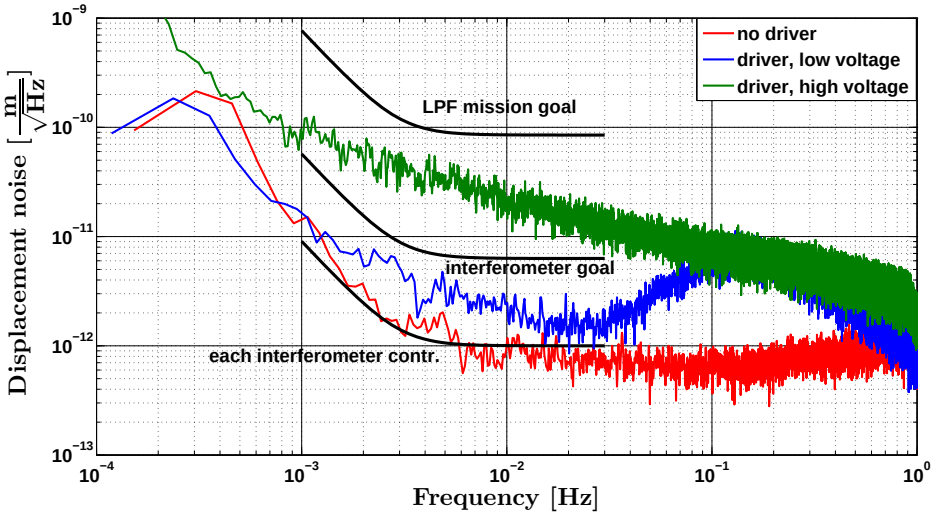

Figure 3.5.: The driver is connected to the piezo and the displacement noise is measured. All control loops are activated. ()The driver might not have been properly terminated without input.)

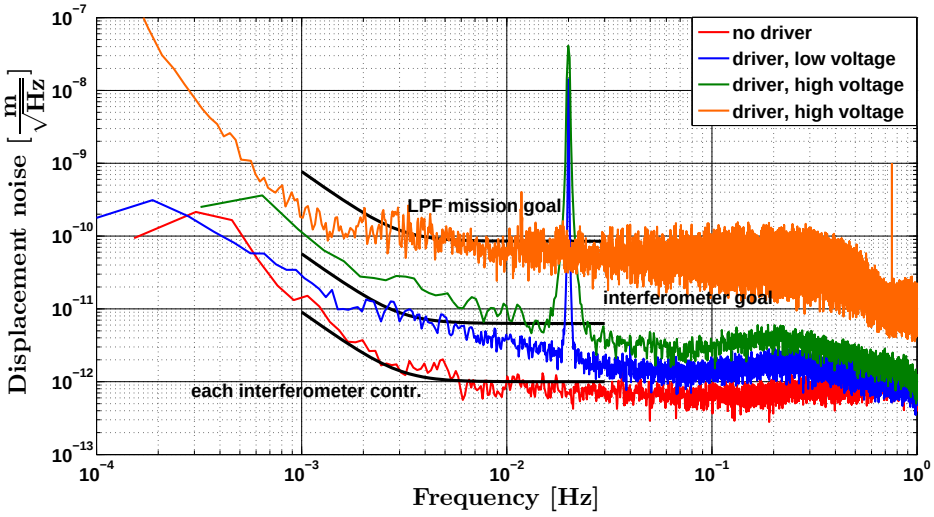

Figure 3.6.: Driver noise with input. The peak of the low voltage input (blue) is at $1.4 \cdot 10^{-8} \frac{m}{\sqrt{Hz}}$, this was produced with a driver input of 20 mHz and 1 mVpp. The peak of the high voltage output (green) is at $4.1 \cdot 10^{-8} \frac{m}{\sqrt{Hz}}$ from a driver input of 20 mHz and 100 mVpp. The orange spectrum was produced with a more relevant high voltage input of 0.00092 Hz and 1 Vpp. The noise level is significantly higher.

3.2. Data analysis

The full MATLAB© script can be found in Appendix A.1; the main parts will be mentioned in this Chapter. The LTPDA toolbox is used during this analysis.

D is an LTPDA analysis object, this file is created from a file containing the recorded time series from the phasemeter. With `omsCalibrateLong` the interferometer signal in radians is calibrated to meters, also the subtraction

$$\Phi_{\mathrm{XM}}[\mathrm{m}] = \frac{4\pi}{\lambda}(\phi_{\mathrm{X1}}[\mathrm{rad}] - \phi_{\mathrm{R}}[\mathrm{rad}])$$

is done in this step. This was mentioned before in Chapter 2.3.2 as an important step to suppress noise common to all interferometers. [17]

```
1 D = ao.load(fullfile(pRoot, datadir, sprintf('data.mat')));
2 Drs = fixfs(D, plist('fs', 32));
3 X = omsCalibrateLong(Drs);
```

The measurement is then cut into shorter segments; an example time series can be seen in Figure 3.7. For each segment a the spectrum is estimated; a range of possible spectra can be seen in Figure 3.8. With a similar loop the mean TM displacement of this segment is calculated.

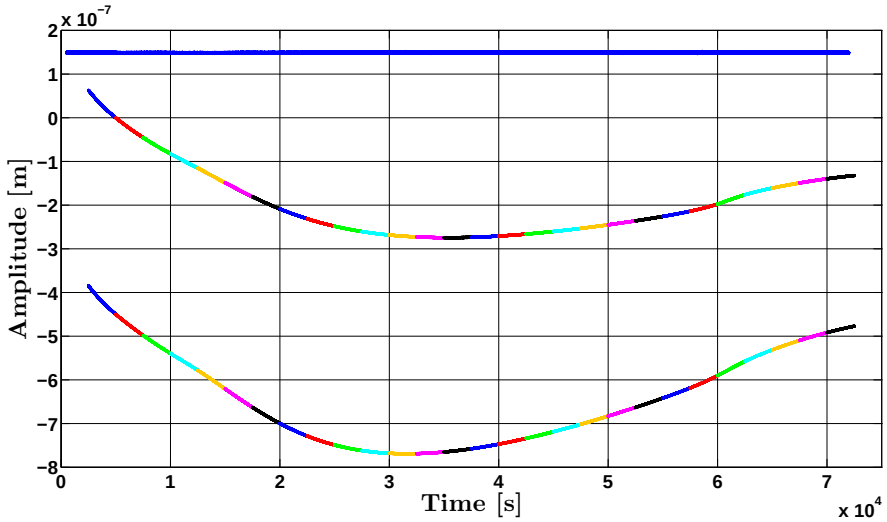

Figure 3.7.: The measurement is cut into segments, these are later used for the analysis of amplitude noise. See Chapter 3.4.4 and Figure 3.17. Natural drift causes a phase difference between the reference signal (blue curve) and the measurement signals (colorful curves, X_1 is above X_{12}).

```
%% Split in times

% number of segments
segs = 94;

%time overlap
ovLap = 1800;
times = zeros(1, segs);

% create times vector
for ii = 1:segs

  times(2*ii-1) = ii*2000+50000;
  times(2*ii) = ii*2000+ovLap+50000;

end

% split the time series
x1_s  = split(X_1_full,  plist('times', times));
x12_s = split(X_12_full, plist('times', times));

%% Loop to calculate the position and spectra

% plist definition
ppl = plist('Kdes',  50, 'order', 1, ...
            'Jdes',  500,'win', specwin('Kaiser', 10, 70),...
            'Scale', 'ASD');

% LPSD of all segments
x1_s_lsd  = lpsd(x1_s,  ppl);
x12_s_lsd = lpsd(x12_s, ppl);

%% Select the frequency
x1_lsd_s  = split(x1_s_lsd,  plist('frequencies',[0.1 1]));
x12_lsd_s = split(x12_s_lsd, plist('frequencies',[0.1 1]));
```

Not the whole spectra is used for the noise analysis, the mean noise level between 0.1 Hz and 1 Hz is calculated. With this information, plots of the noise over time and position can be done. Example plots can be seen in the following chapters.

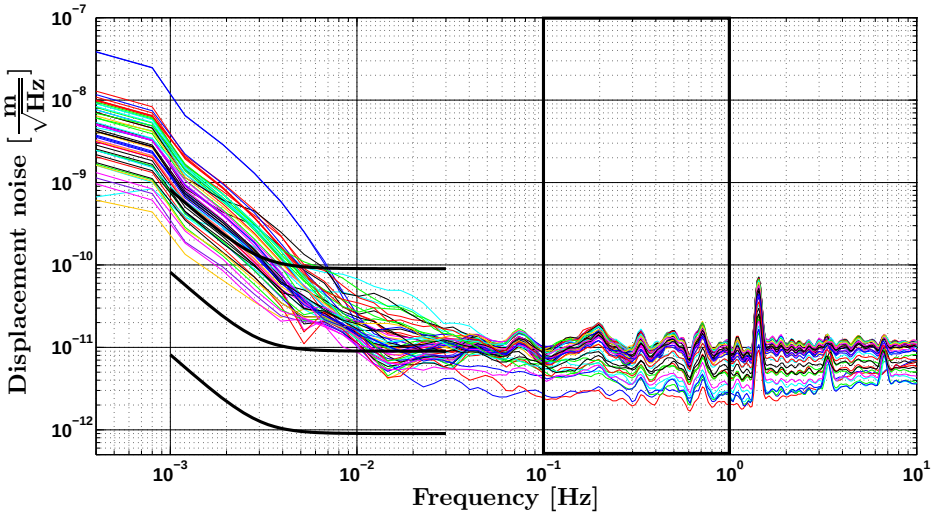

Figure 3.8.: For each segment the spectrum is estimated and the frequency range indicated by the rectangle is used for further noise analysis. In this the measurement excess amplitude noise is injectd to dominate the measurement above 10 mHz.

3.3. Noise dependence on absolute path length: theoretical predictions

The noise level not only depends on the loop setups of the system, but also on the macroscopic relation between the measurement and reference interferometers. Common mode noise is removed by subtracting the reference signal from the measurement signals. The efficiency of the subtraction depends on the phase between reference and measurement signal. Chapter 3.3 focuses on the theoretical predictions, which were first discussed during the test campaigns where some experiments were done [17]. Recently Gerald Hechenblaikner from EADS Astrium wrote a paper on this topic, most of the information in this subsection was taken from that paper.[18] In Chapter 3.4 the predictions will be tested in experiments.

The interference of the measurement and reference beams is measured by the photodiodes. These signals are then sent to the phasemeter. This signal contains phase and amplitude noise from the two beams. Since the same beams are used on the reference interferometer we have another signal which differs only by the test mass motion. Recall

$$\begin{aligned}
\Delta\phi_{\mathrm{X1}} &= \delta\phi_{\mathrm{TM1}} + \delta\phi_{\mathrm{OB}} + \delta\phi_{\mathrm{common}} + \delta\phi_{\mathrm{differential}},\\
\Delta\phi_{\mathrm{X12}} &= \delta\phi_{\mathrm{TM1}} - \delta\phi_{\mathrm{TM2}} + \delta\phi_{\mathrm{OB}} + \delta\phi_{\mathrm{common}} + \delta\phi_{\mathrm{differential}},\\
\Delta\phi_{\mathrm{XR}} &= \delta\phi_{\mathrm{OB}} + \delta\phi_{\mathrm{common}} + \delta\phi_{\mathrm{differential}}.
\end{aligned}$$

The main interest is the motion of the test mass, so the common mode noise is suppressed by subtracting the reference interferometer signal from the measurement interferometer signal. The efficiency of this subtraction, however, depends on the phase between the two signals.

3.3.1. Amplitude noise

A sinusoidal digital signal with a sampling frequency of f_{samp} is affected by amplitude noise. This noise has uniform linear spectral density $n_{\mathrm{ld}}\,[\frac{V}{\sqrt{\mathrm{Hz}}}]$, which causes the signal sampling steps to fluctuate. n_{k} are uncorrelated distinct random variables with a uniform linear spectral density with

$$\begin{aligned} \langle n_{\mathrm{k}} \rangle &= 0, \\ \sqrt{\langle n_{\mathrm{k}} n_{\mathrm{m}} \rangle} &= \delta_{\mathrm{km}} n_{\mathrm{ld}} \sqrt{\frac{f_{\mathrm{samp}}}{2}}. \end{aligned}$$

The effect of this amplitude noise on the phase error at the phasemeter output was calculated, the uniform spectral density of the phase noise is

$$\mathrm{LSD}(\Delta\Phi_{\mathrm{Amplitude}}) \;=\; \frac{n_{\mathrm{ld}}\sqrt{2}}{A_{\mathrm{in}}},$$

where A_{in} is the amplitude of the input signal.
Two signals with phase noise caused by common mode amplitude noise are subtracted to suppress this noise. N is the number of points of the FFT. The two signals have a phase difference of Ψ, the mean square fluctuations of the phase meter output, n, can be calculated to be

$$\langle \Delta n^2 \rangle \;=\; \frac{2}{N\,A_{\mathrm{in}}^2} \langle n_{\mathrm{k}}^2 \rangle 4 \sin^2 \frac{\Psi}{2}.$$

The minima of the common mode amplitude noise of the subtracted signal can be found by a phase difference Φ of 0 or 2π between measurement and reference signal.

3.3.2. Phase noise

The phase noise has similar properties to the amplitude noise. The fluctuations of the sampling steps are again uncorrelated and have a uniform spectral density. Again two signals with a phase difference of Ψ are subtracted, and the mean square value of the phase noise at the phase meter output n yields:

$$\langle \Delta n^2 \rangle \;=\; \frac{2}{N} \langle n_{\mathrm{k}}^2 \rangle 4 \sin^2 \Psi.$$

The phase noise has minima at a phase difference Ψ of 0, π and 2π. At a phase difference of $\frac{\pi}{2}$ the phase noise is maximal (see Figure 3.10).

3.3.3. Digitisation noise

A third effect, reported by colleagues in Glasgow, occurs in the phasemeter. In the phasemeter the signal is digitised with a frequency of 32.4Hz. This leads to an uncertainty in the phase information. The relevance of this uncertainty depends on the amplitude of the phase during the subtraction of the reference signal from the measurement signal, depending again on the phase difference between these two signals. An experiment with two frequency locked function generators (with variable phase difference) is planned to explore this effect.

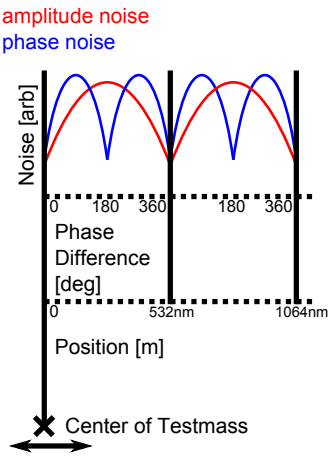

Figure 3.9.: An attempt is made to connect test mass motion with the noise at different TM positions. When the test mass is moved [x-axis in nm], the path length of the measurement beam changes, thus the phase of the measurement signal changes. The phase difference between measurement signal and reference signal [x-axis in deg] obviously changes as well, and the dependence of amplitude and phase noise becomes visible.

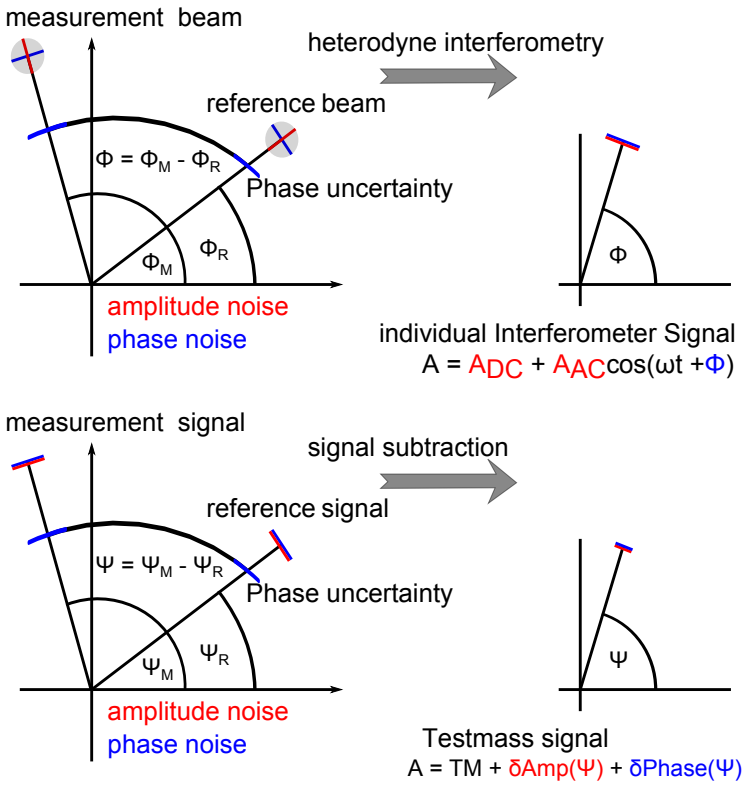

Figure 3.10.: Laser beams and signals are presented in the phasor picture. In the top figure two beams are interfered on a photodiode, the result is a signal which is transferred to the phasemeter. In the bottom figure two signal are subtracted. The result is a new signal, where ideally the common mode noise is suppressed. The common mode noise which was not subtracted depends on the phase between the two signals.

3.4. Noise dependence on absolute path length: experiments

In the experimental setup we start at an arbitrary phase difference between measurement and reference signals. The fringe is scanned by moving the measurement phasor, since the reference interferometer is fixed. A scan over the whole fringe 2π can be achieved in two ways.

The obvious approach is to move the test mass mirror. Since the reference beam is fixed, the optical path of the measurement beam has to be moved by 1064nm. This corresponds to TM mirror motion of 532nm. This movement can't be achieved with the low voltage output of the driver, so experiments were done with the high voltage output. Since this did not show the noise behaviour we expected different approaches were taken. This is likely due to the two signals being dominated by motion induced by driver noise, and not dominated by either amplitude or phase noise. The following sections describe the investigation process and the results.

3.4.1. Test mass motion with a function generator

The first approach was with the Stanford function generator which was used in Chapter 3.1.2. Motion with a period of 10 hours was induced, this long measurement duration guarantees a roughly constant macroscopic test mass position over the segment where we calculate the noise.
As expected from previous noise investigations the high noise of the high voltage setup and the unavoidable steps from the function generator made it impossible to see the common mode noise subtraction efficiency.

When the noise position is plotted over TM position folded into a range from 0 to 2π no clear shape is visible. If, however, the noise is plotted over time together with the position of the test mass it can be seen that the noise level depends on the output voltage of the driver. This pattern is independent of the test mass position and solely depends on the voltage input to the driver.
The cause for this peculiar noise-shape is currently unknown to me. It is independent of the maximum amplitude as can be seen in Figures 3.11 and 3.12 where the TM motion is shown together with the noise. I suspect frequency fluctuations from the amplifiers, see Figure 3.13. A comparison of the motion range of the test mass in these two measurements can be seen in Chapter 3.1.2 in Figure 3.3 where the range of high and low voltage driver output are compared. Another problem of the setup are the digitization steps of the function generator (see Figure 3.14) which produces a broadband noise.

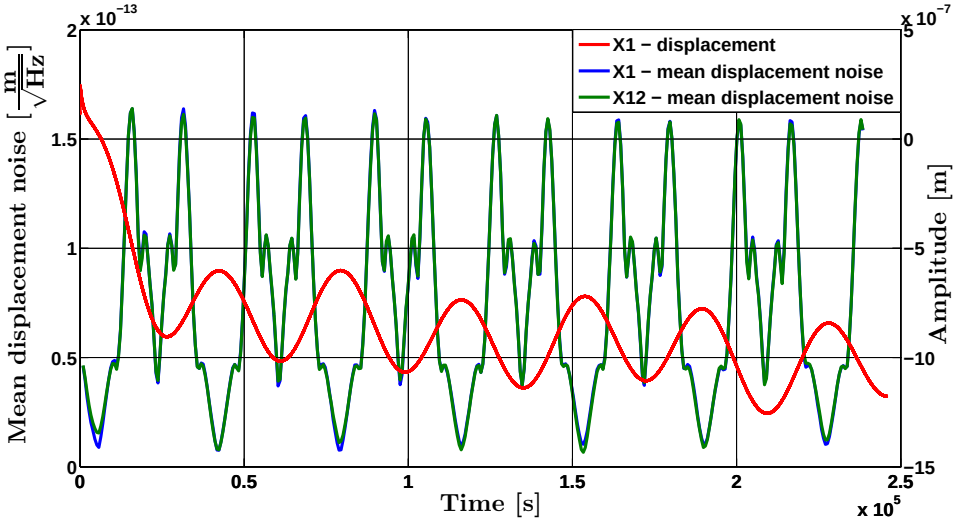

Figure 3.11.: The red curve shows the motion of test mass 1 (right y-axis, less than $0.5\,\mu$m) over time. The mean displacement noise between 0.1 Hz and 0.1 Hz (left y-axis) is calculated with the algorithm from Chapter 3.2 and plotted over time. The segments for this noise calculation overlap for a higher resolution.

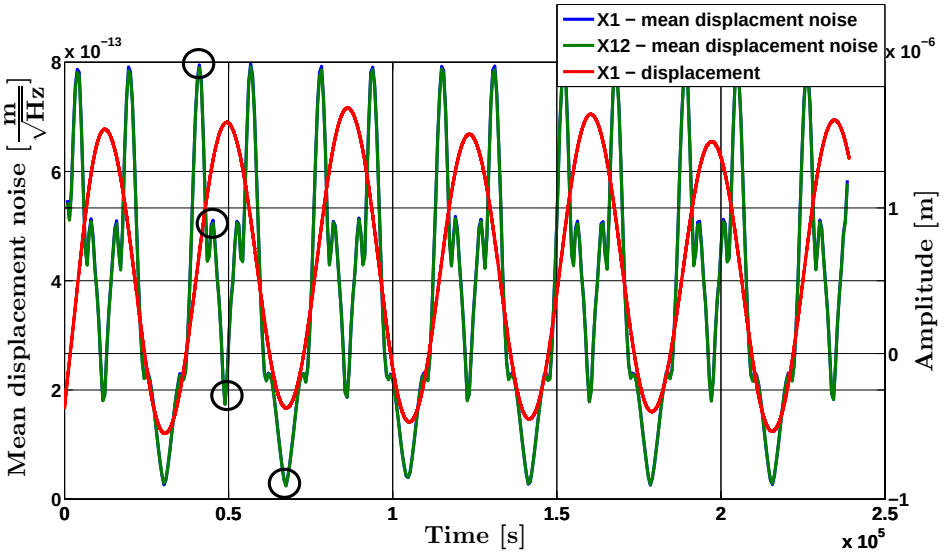

Figure 3.12.: This noise curve is calculated with the same method as in Figure 3.11, but here TM motion is bigger ($2\,\mu$m) and the maximum mean noise level is higher. The behaviour of the noise is still the same although the test mass motion range differs by a factor of 4.

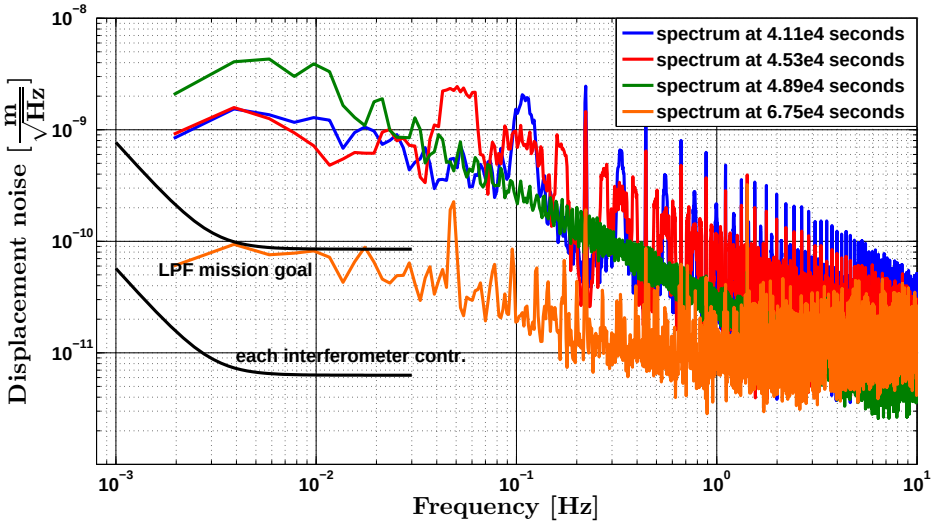

Figure 3.13.: Example spectra of the plot in Figure 3.12 at the time indicated by circles.

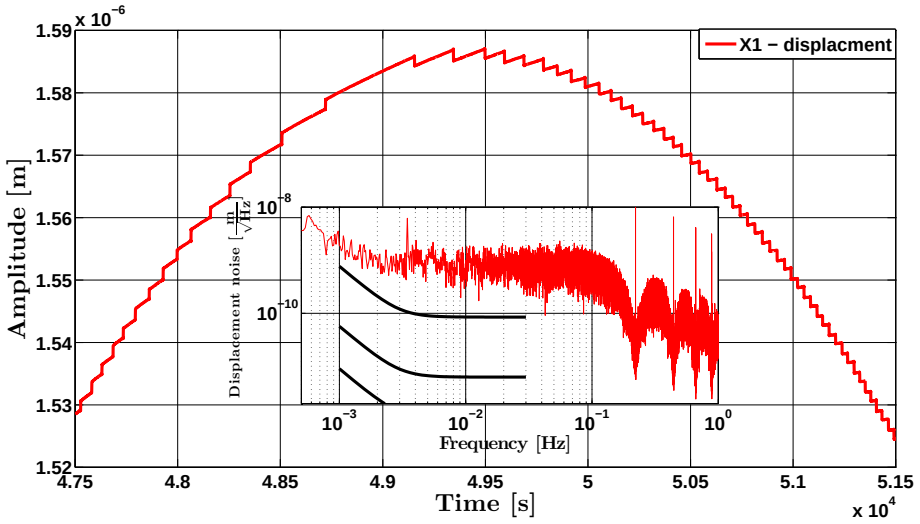

Figure 3.14.: The function generator doesn't provide a continuous sine function, rather it consists of small voltage steps. This leads to a broadband noise with strong peaks, as can be seen in the higher frequency region.

3.4.2. Test mass motion with a DC power supply

The next approach was to use a DC Voltage supply. The voltage is changed by the lab computer. This reduces the number of points, but has the advantage of greatly reducing the uncertainty in the position since the driver output voltage is stable over each time segment analysed. A trade-off for the step size between a reasonable number of measurement points and a realistic measurement duration was made. The natural drift over day and night is much larger than the motion produced by the steps. The purpose of the step is to make fixed discrete phase offsets, however with this drift this is not possible (see Figure 3.15).

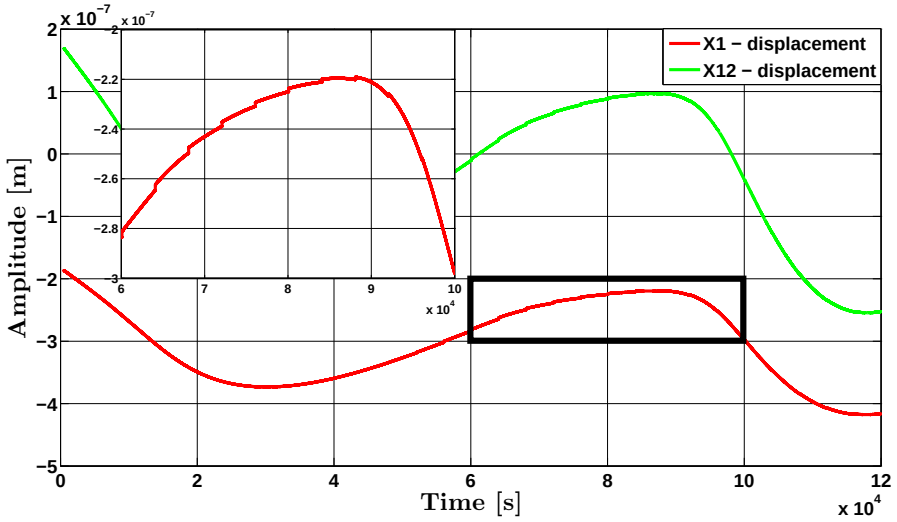

Figure 3.15.: A DC power supply is used to move the piezo, the TM motion due to thermal fluctuations over the day is much larger than the input voltage steps.

3.4.3. Laser frequency manipulation

The driver and piezo produce excess noise, but there is another way to change the phase difference of the signals. One of the reasons that frequency control is necessary is that a change in frequency leads to a signal looking like a test mass movement:

$$\delta x = \frac{\delta\nu}{\nu}\delta L,$$

where δx is the apparent path length fluctuation, $\delta\nu$ is the laser frequency noise and δL is the path length difference between measurement and reference beam (see Chapter 2.3.3).
This can be used to generate a signal with a phase change over many radians in the course of a long term measurement.
Unlike motion of the test mass the frequency drift is measured by the reference interferometer as well. The actual path length difference of the reference interferometer

δL_r of the ground setup is non-zero, but different from the path length difference of the measurement interferometer δL_m. This yields a phase change between measurement and reference signal of

$$\delta\phi = \frac{4\pi}{\lambda}\frac{\delta\nu}{\nu}(\delta L_\mathrm{m} - \delta L_\mathrm{r}) = \frac{4\pi\,\delta\nu}{c}(\delta L_\mathrm{m} - \delta L_\mathrm{r}),$$

where c is the speed of light. An example for the phase change between measurement and reference signal over the course of several hours can be seen in Figure 3.7.
The slow frequency loop controls the temperature of the laser crystal. Input voltages between $-10\,\mathrm{V}$ and $10\,\mathrm{V}$ can be chosen as input to heat or cool the crystal. Different inputs from a function generator and a DC power supply were tested (see Figure 3.16). It turned out that the natural drift, which occurs over the duration of the measurement when the loop is turned off, is sufficient for our purposes. One example for frequency drift without the slow frequency loop can be seen in Figure 2.11. The fast frequency control loop is still turned on. A comparison of the frequency drift with and without control loop can be seen in Chapter 2.3.3 Figure 2.11.
All following experiments were performed with this setup. Additional amplitude or phase noise was introduced into the system to obtain information about their behaviour.

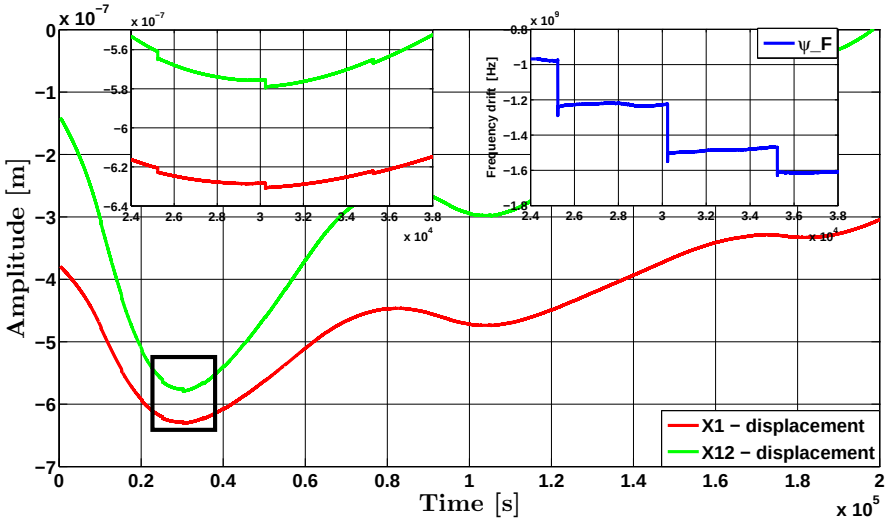

Figure 3.16.: The step function is clearly visible in the output of the frequency interferometer (blue), the impact of the step function on the phase difference between measurement and reference signal is limited, which can be seen in the time series of X1 and X12 (red and green).

3.4.4. Amplitude noise

The amplitude noise control loops are turned off, and amplitude noise is not dominating the system in the measurement band. Therefore the AOMs are connected to a function generator which produces white noise at a level which causes the amplitude noise to dominate other sources, allowing the predicted behaviour to be seen

The predicted behaviour takes the form

$$\langle \Delta n^2 \rangle = \frac{2}{N A_{\mathrm{in}}^2} \langle n_{\mathrm{k}}^2 \rangle 4 \sin^2 \frac{\Psi}{2}.$$

can be seen (see Figure 3.17). A fit of this functional form to the data yields:

$$\begin{aligned} \mathrm{X1}: &\quad 9.32822 \cdot 10^{-5} \cdot \sin^2 \tfrac{\Psi}{2} + 2.7478 \cdot 10^{-5}, \\ \mathrm{X12}: &\quad 11.9628 \cdot 10^{-5} \cdot \sin^2 \tfrac{\Psi}{2} + 3.4488 \cdot 10^{-5}. \end{aligned}$$

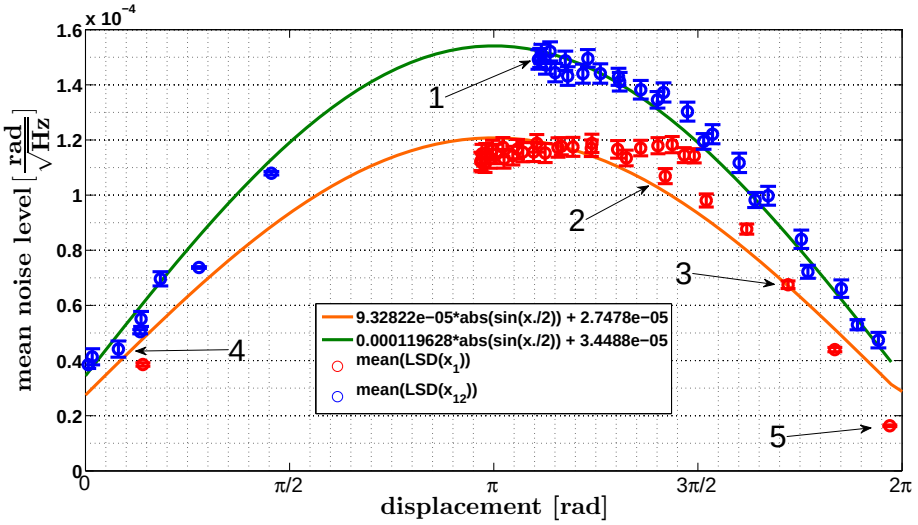

)

Figure 3.17.: Additional amplitude noise was fed into the system, although the natural drift was not enough to show the full $\sin^2 \frac{\Psi}{2}$ curve an estimate for the maximum mean amplitude noise can be made. Spectra for the points indicated by arrows can be seen in Figure 3.18.

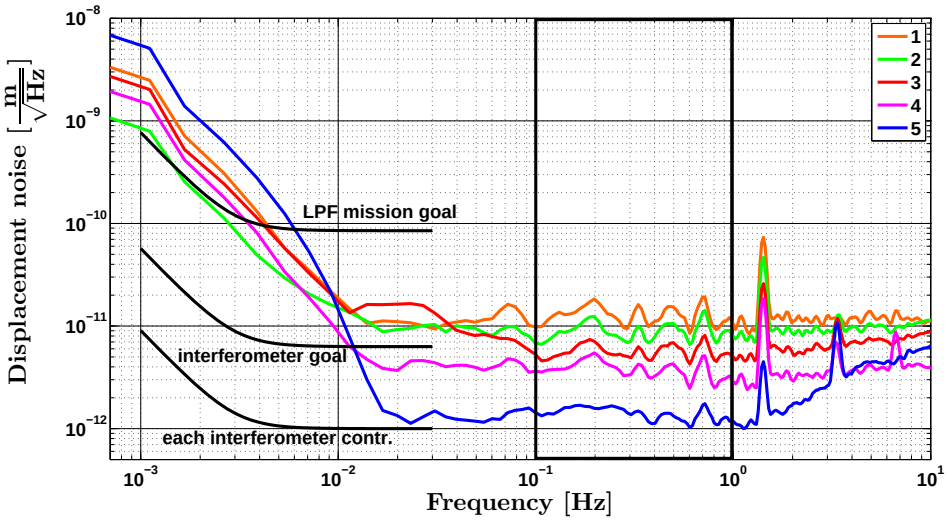

Figure 3.18.: Additional amplitude noise was fed into the system, although the natural drift was not enough to show the full $\sin^2 \frac{\Psi}{2}$ curve an estimate for the maximum mean amplitude noise can be made.

3.4.5. Phase noise

The ground setup provides enough phase noise when the OPD Loop is turned off (see Chapter 2.3.2). The differential phase noise between the two beams is now common to all interferometers and is then subtracted. The predicted noise shape

$$\langle \Delta n^2 \rangle \;=\; \frac{2}{N} \langle n_{\mathrm{k}}^2 \rangle 4 \sin^2 \Psi$$

could be observed easily. The maximum mean phase noise is about one order of magnitude higher than the maximum amplitude noise. This is consistent with Chapter 2.3 where the control loops and noise levels were investigated.
The functions determined by a fit algorithm yield

$$\begin{aligned} \mathrm{X1} &: 0.00160753 \cdot \sin^2 \Psi + 5.6105 \cdot 10^{-5}, \\ \mathrm{X12} &: 0.00153866 \cdot \sin^2 \Psi + 12.514 \cdot 10^{-5}. \end{aligned}$$

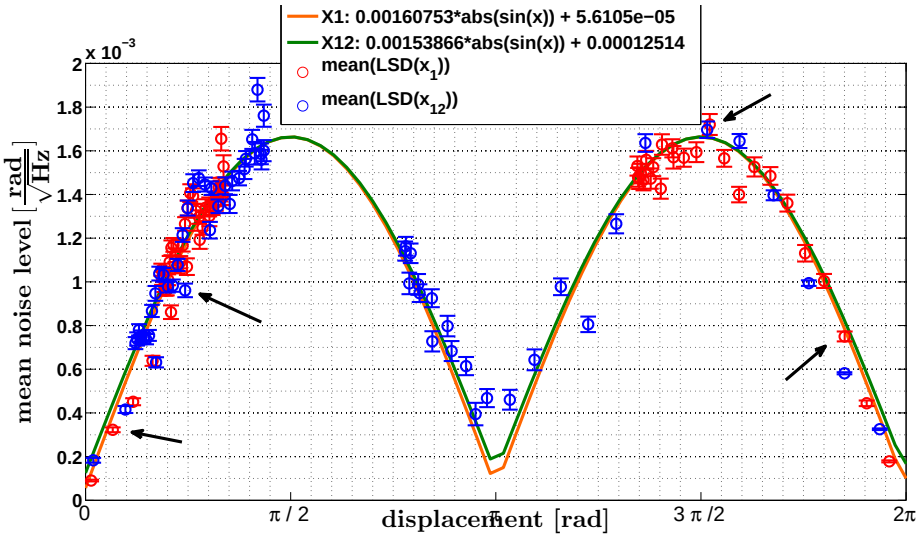

Figure 3.19.: The $\sin^2 \Psi$ noise shape can be observed. The reason for the higher noise at π might be due to amplitude noise, but it has to be considered that the maximum mean amplitude noise measured before is only half of this noise floor of this measurement. Additionally the phase difference has an uncertainty of $\pm n \cdot \frac{\pi}{2}$, n integer. The arrows indicate the points which belong to the spectra in Figure 3.20

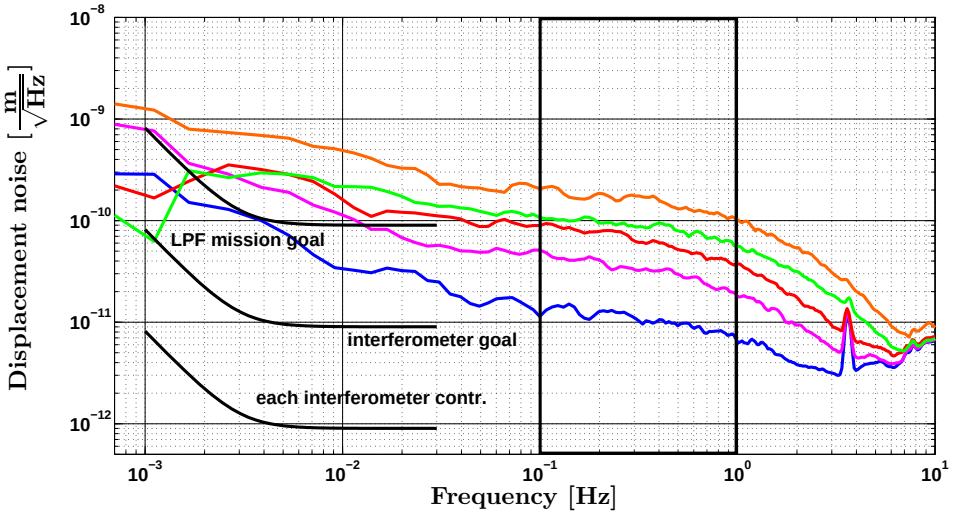

Figure 3.20.: These spectra show the noise level at the positions indicated in Figure 3.19. The mean value of the spectrum in the rectangle is used for further analysis, the different noise levels can be seen. Excess phase noise was introduced into the system.

3.4.6. Amplitude and phase noise

Since the maximum mean phase noise level is one order of magnitude bigger than the mean maximum amplitude noise it is makes it difficult to measure a combination of both noise shapes. To reduce the amount of phase noise the OPD loop was turned on again, an intentionally low loop gain was chosen so that not all phase noise is suppressed. This experiment depends very much on random factors like frequency drift and environmental phase noise level changes, the results are not totally convincing.

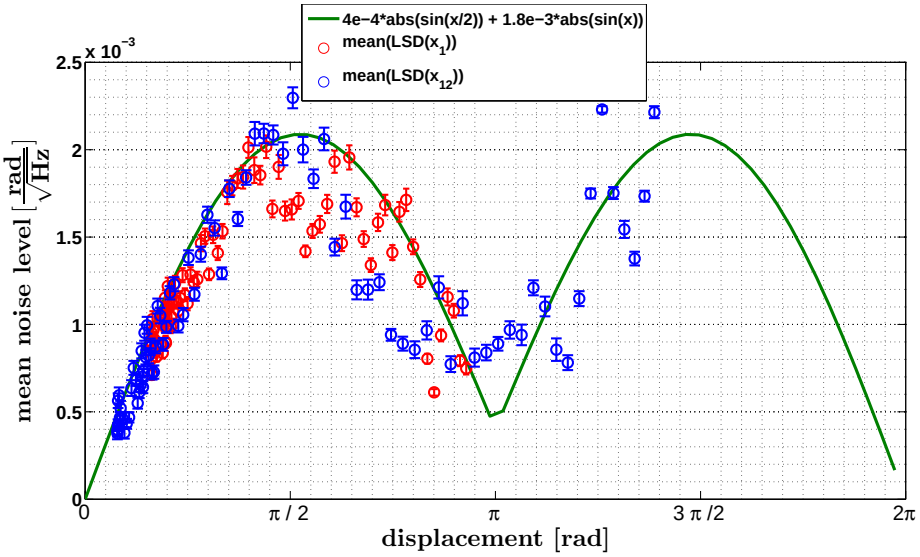

Figure 3.21.: The phase noise is clearly dominating, the OPD loop is turned on but the loop performance is intentionally bad. It is unlikely that the origin of the peak at π is due to amplitude noise since the noise level is at $0.8\,\frac{\mathrm{mrad}}{\sqrt{\mathrm{Hz}}}$.

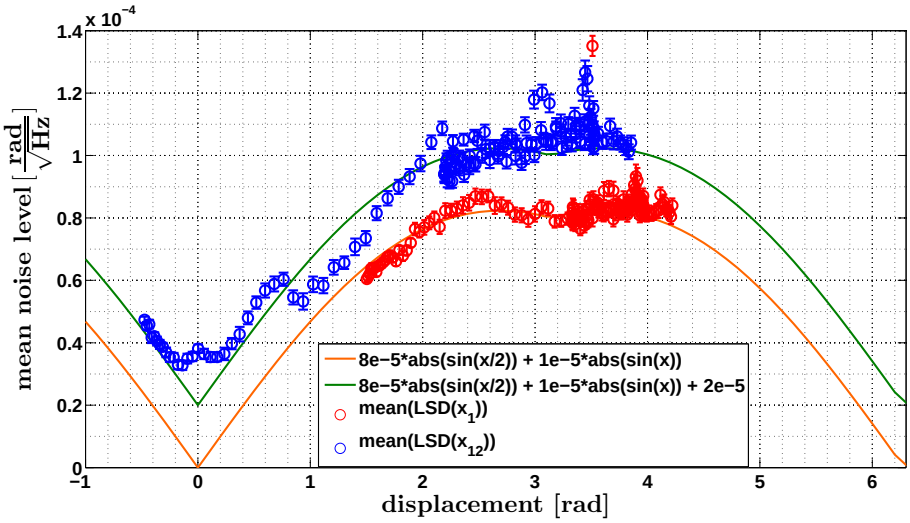

Figure 3.22.: A similar bad setup of the OPD Loop as in Figure 3.21 is used, amplitude and phase noise seem to be at a similar noise level.

3.4.7. Conclusions

There is clearly some dependence of the efficiency of the amplitude and phase noise subtraction on the phase difference between the reference and measurement interferometer, as predicted by Gerald Hechenblaikner was measured.

Similar measurements were done during the test campaigns. [17]These were explained with first and second order side-bands on the laser beams. These side-bands have a frequency difference of f_{het} and interfere on the recombination beam splitters, leading to amplitude and phase noise. Calculations of their impact on the performance showed a sinusoidal dependence on the phase difference between the two signals as well. The origin of the laser frequency side bands was found in electric cross-coupling between the AOM driver circuits. [13]
Hechenblaikner begins his derivation with fluctuations of digital sampling steps. The experiments could be redone with an analog subtraction of the reference signal from the measurement signals. The signal used in the frequency control loop is the result of an analog subtraction of the reference signal from the frequency signal, the efficiency of the ground setup frequency control might depend on the path length difference between reference and frequency interferometer.

4 Electrode housing mockup

Interferometric measurement is not the only way the test mass position is measured. Test mass displacement sensing along the sensitive axis is the main science output, since this enables the measurement of gravitational waves in the LISA mission. However, for successful navigation of the satellite, information about all axes is necessary. All degrees of freedom are sensed by capacitive readout.
Around the test mass an electrode housing is built, and the measurement beam has to travel through a hole in this housing twice. Our ground setup has no such housing, and so for this thesis a mockup was designed to simulate the beam aperture and reflective properties of the flight model electrode housing.
The objective of this experiment is to determine the influence of the housing on the noise performance and contrast of the individual interferometers. In the first section the design and operation of the housing is described; in the second section performance measurements with different setups are compared.

4.1. Design

For the design process the dimensions of the flight hardware were gathered from official documentation, and the nominal position for the test mass in flight was calculated for the ground setup. With this used as reference the design parameters for the housing were calculated. This chapter describes the housing mockup design process and operation of the device.

4.1.1. Test mass mirror position

In the satellite the test mass and capacitive actuators are placed inside a vacuum chamber, and the laser beam travels through a window. The vacuum chamber isolates the vacuum around the TM from the vacuum of the space craft and optical bench (Figure 4.1).
The ground setup has no extra vacuum tank and no window. Without the window the beam is parallel shifted and has a shorter optical path length due to the lower refractive index of vacuum compared to glass. The necessary TM shift to reproduce the beam path was computed to be 1.58 mm (see Figure 4.2). [13]
For alignment purposes the GUI shows the position of the X_1 and X_{12} interferometer measurement beams on the QPDs, the test mass is moved to the point of maximum

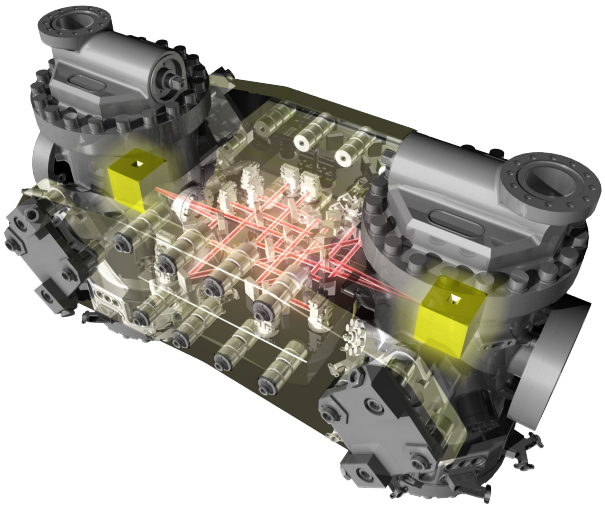

Figure 4.1.: The optical bench is placed in the middle of the satellite, the interferometers are identifiable through the red laser beams. These hit the test masses (gold), around each test mass an electrode housing is build. This is placed in a vacuum tank to separate the vacuum of the test mass from the spacecraft. On the way to the test mass the laser beam travels through a window in the vacuum tank and a hole in the electrode housing.

contrast of the two beams. If the test mass is placed in the nominal position the point of maximum contrast is in the centre of the QPD, where the measurement beam and reference beam are parallel. The test mass is placed and aligned by hand. The longitudinal shift from the nominal position can be seen on the GUI as beam movement in the horizontal direction on the QPD.
In the flight hardware the TM vacuum tank window is tilted in η at an angle of $2.5° \pm 0.075°$to avoid backscattering. Similar to the previous parallel shift of the beam, this tilt of the window leads to a parallel shift vertical to the OB surface of $99.86\,\mu$m. [19] Since the window is missing the free beam does not experience such a shift, an offset is visible on the QPD panel of the user interface. The beam position of maximum contrast is slightly above the centre of the QPD.
A rectangular casing was designed to place the optical bench safely in the vacuum tank; it also holds the piezos with the test mass mirrors. It is made of zerodur to guarantee the same temperature behaviour as the OB and avoid strain.
This OB casing is used as reference, and the test mass nominal position without the window was calculated. The following numbers were used:

- Distance from the centre of the optical bench (COB) to the surface of the test mass in the nominal position: 165 mm, with window (CAD model).
- Distance from the COB to the surface of the test mass in the nominal position: 163.42 mm (without window, from [20][13]),
- Distance from the COB to the surface of the test mass in the nominal position: 162.72 mm(without window, from [19]),

- Distance from the COB to the surface of the zerodur case: 161.8 mm (from [21][22]),
- Distance between the surface of the test mass and the surface of the zerodur case: −1.62 mm or −0.93 mm.

The test mass was placed near this position. A measurement with all loops showed a similar noise performance.

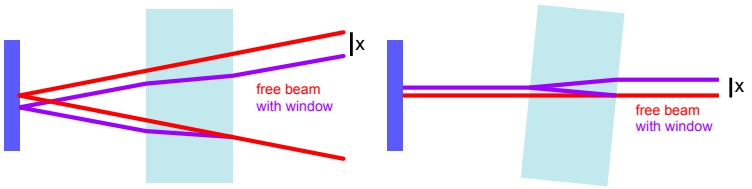

Figure 4.2.: In the flight interferometer a window is placed in front of the test mass. The beam path (purple) is diffracted by the higher refractive index of the glass. The red beam shows the path without the window; this is the case in the ground setup. The two outgoing beams are parallel. The left picture shows the beam paths in plane with the optical bench surface, to reproduce the path on the ground the test mass has to be moved 1.58 mm away from the optical bench. The right picture shows the beam path perpendicular to the OB surface, the vertical beam shift was computet to be $x = 99.86\,\mu$m.

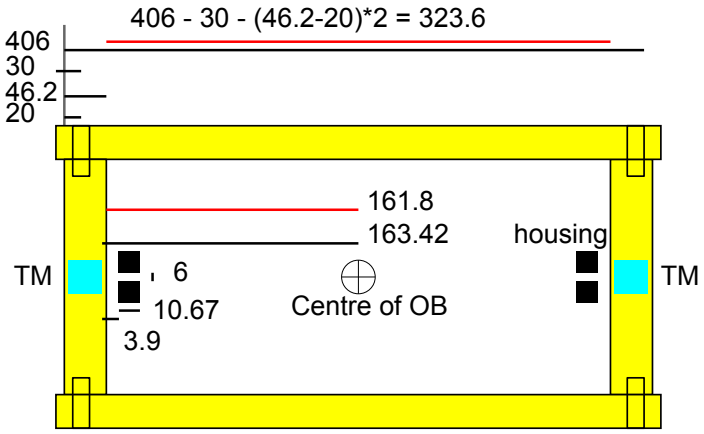

Figure 4.3.: The optical bench is placed in the centre of this case(yellow), the test masses are secured at the left and right side. In front of the test mass the housing mockups are placed. Dimensions were taken from [22], [20] and [21] .

4.1.2. Design process

The incoming beam hits the test mass with an angle of 4.5 deg and has to travel through the hole of the electrode housing, hit the test mass, and travel back out again.
Of potential importance is scattering on the outside of the housing, which might travel parallel to the measurement beam and reach the photodiode. Also light might hit the inside surface of the housing or the inner walls of the hole, and travel out in various directions.If this light hits the photodiode it will lead to more noise.
The electrode housing hole of the flight model has a diameter of 6 mm and a depths of 10.67 mm, the inner surface of the housing has a distance of 3.9 mm from the test mass in the nominal position (see Figure 4.5 and [23]).
The housing mockup has to be placed very precisely to ensure representative results. The optical bench and the test mass mirrors are screwed to a zerodur casing, which is used as a reference for the position of the hole.
The OB casing panels where the TM mirrors are placed have a hole, from the rear side the piezo is put in place. The TM mirror protrudes out of the front surface of the casing.
A special alignment device was designed which fits in the back side hole of the piezo holding. This device protrudes out of the front hole, the housing mockup is designed to fit exactly on this. This way the OB casing is used as reference for the alignment of the housing. A limitation for the accuracy can be estimated with the accuracy of the case, the documentation claims an accuracy of 0.5 mm. The little circular hole of the housing mockup was drilled in the same session as the bigger hole on the rear end which is used for alignment, the accuracy is limited by the reproducibility of the driller position.
Once the housing is placed it is secured with screws to the optical bench casing.
The housing mockup is aligned like this:

- Remove the piezo and the TM mirror;
- Mount the housing mockup on the OB case and adjust it to the alignment device;
- Secure the housing mockup with the screws;
- Remove the alignment device and put the TM mirror back in;
- Confirm the longitudinal position with the alignment stick, then align the TM as usual;

The housing mockup can be removed without touching the mirror by sliding it sideways. Performance measurements with different setups were done; these are described in the following chapter.

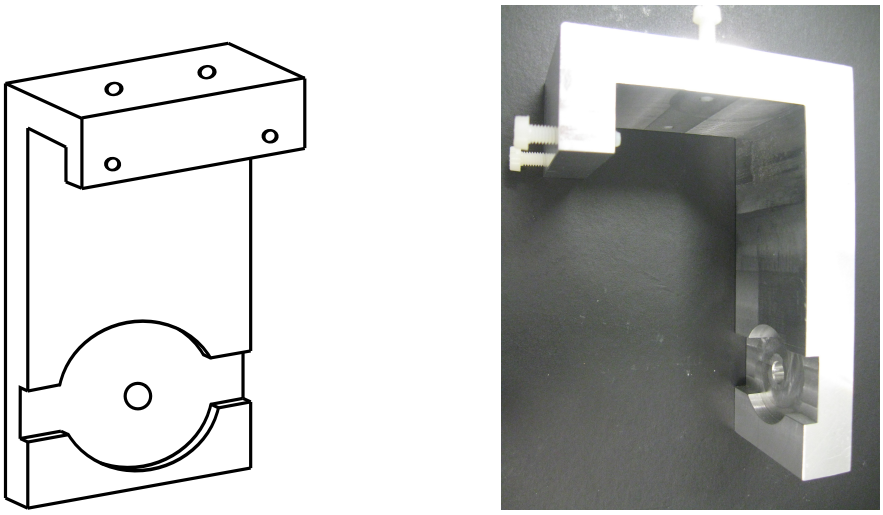

(a) Design **(b)** Photograph

Figure 4.4.: For the purpose of this experiment it is sufficient to simulate the housing with a polished aluminium piece with a hole, dimensions are the same as in the flight model.

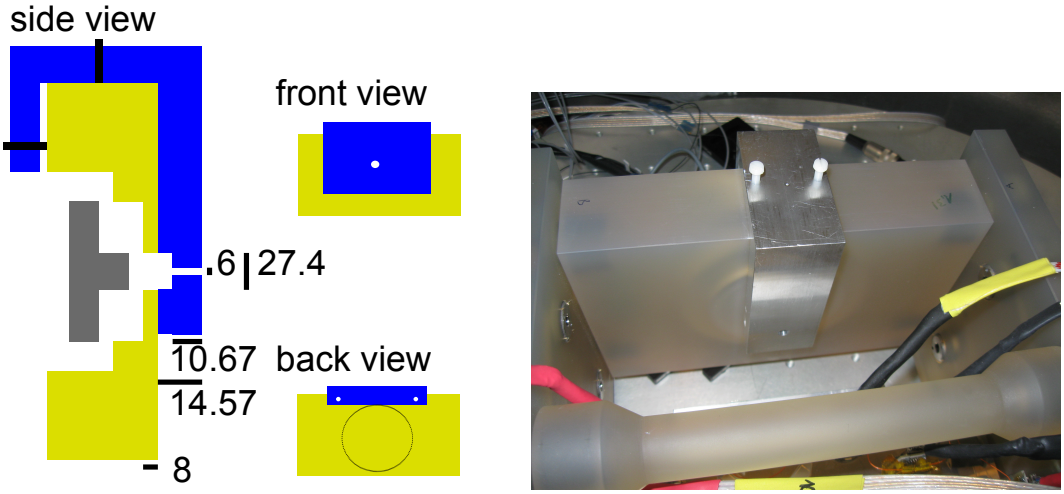

(a) Design **(b)** Photograph

Figure 4.5.: This is the design sketch for the housing mockup (blue or aluminium), it is placed on the OB casing (yellow) in front of the test masses on both sides of the optical bench. The side view also shows the alignment device (grey) and how it is used to ensure an accurate position.

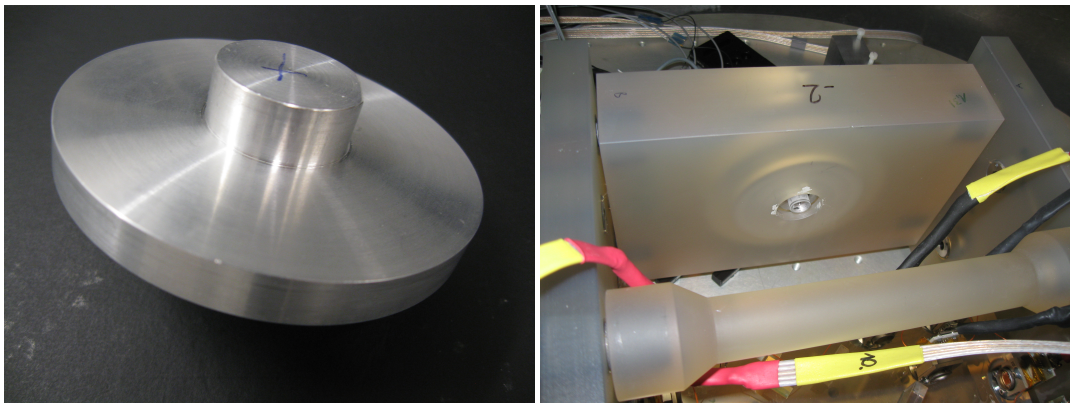

(a) Alignment device **(b)** Test mass

Figure 4.6.: The left picture shows the alignment device, it consists of two cylinders and an handle on the back side. The right picture shows the test mass without housing.

4.2. Performance measurement with housing mockup: stationary measurement

During the alignment process of the housing mockup the TM mirror has to be removed. Therefore the performance measurement with the housing was done first. Without adjusting the mirror the mockup was removed and another performance measurement was done. In between the tank has to be opened and pumped down again, which involves vibrations from the vacuum pump.

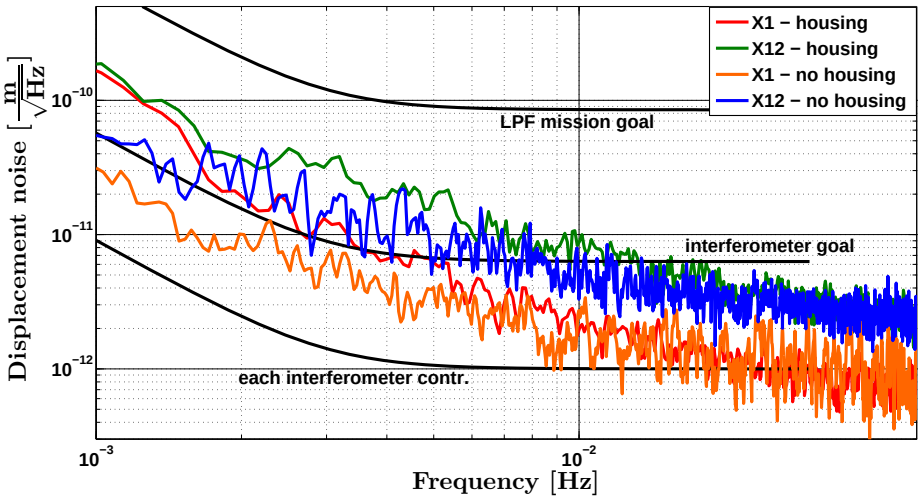

Figure 4.7.: The X_1 interferometer is shown in red and orange; the X_{12} in blue and green. Above 0.01 Hz the noise level is similar; at lower frequencies the noise of the measurements with housing shows higher noise, the difference is in the range of performance fluctuations between different measurements.

The performance of the measurement with housing is worse than previous measurements. The contrast of the interferometers compared to previous measurements is lower. Without the housing contrasts between 70 and 82 on X_1 and between 65 and 72 on X_{12} can be achieved, with around 80 on the reference interferometer. With similar reference interferometer contrast and with the housing the contrast on X_1 is in a similar range, the contrast on X_{12} however is down to 55. The TM2 housing was positioned two times with similar contrast, more experiments should be done.

The spectra of Figure 4.7 were calculated over the whole measurement duration. The test mass drifts even without input due to temperature fluctuations, a weekend measurement with both housings was performed. The test mass motion ca be seen in Figure 4.8, all control loops activated. Over the course of the measurement the performance of X_{12} is worse than of the X_1 interferometer, an experiment where the housings are exchanged is planned.

4.3. Motion measurement

Experiments where the test mass was moved were performed. The effect of the housing is difficult to separate from other effects, especially from the noise dependence of longitudinal test mass position (See Chapter 3) and driver and function generator noise.
Similar to the noise investigation before the mean noise level between 0.1 Hz and 1 Hz was plotted over time, together with the test mass motion.
The test mass was moved with both high and low voltage input to the piezo. With the high voltage output of the driver motion of the TM mirror with intentionally large angular and longitudinal beam jitter was introduced.

4.3.1. Longitudinal motion

TM motion
Motion measurements with both housings were performed. Longitudinal movement of the test mass with both housings showed a similar noise shape of both interferometers, similar to previous measurements the noise is dominated by excess noise from the driver setup (see Chapter 3.4.1).

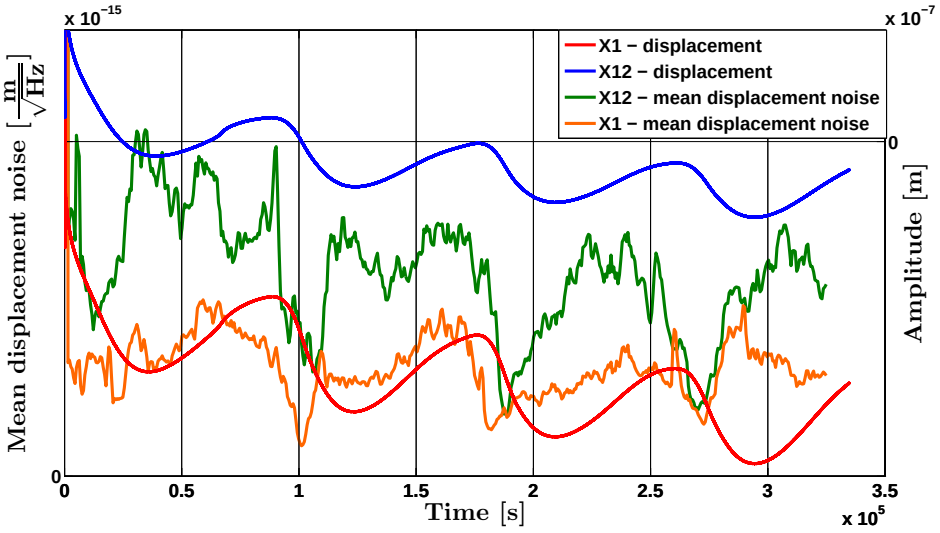

Figure 4.8.: The X_1 interferometer is shown in red, the X_{12} in blue. The corresponding y-Axis is on the right. The noise level over time for this measurement is shown in orange and green. The X_{12} noise level is higher than X_1, the origin of the main contribution to the noise level change over time is most likely due to environmental noise changes (see Figure 4.9).

The housing on TM1 was removed, but left on TM2. Then TM1 was moved with the piezo to measure the effect of reflections on the surface of the TM2 housing. No difference between the two measurements could be seen. The housing on TM2 has no effect on the jitter noise in all observed cycles, one of them is shown in Figure

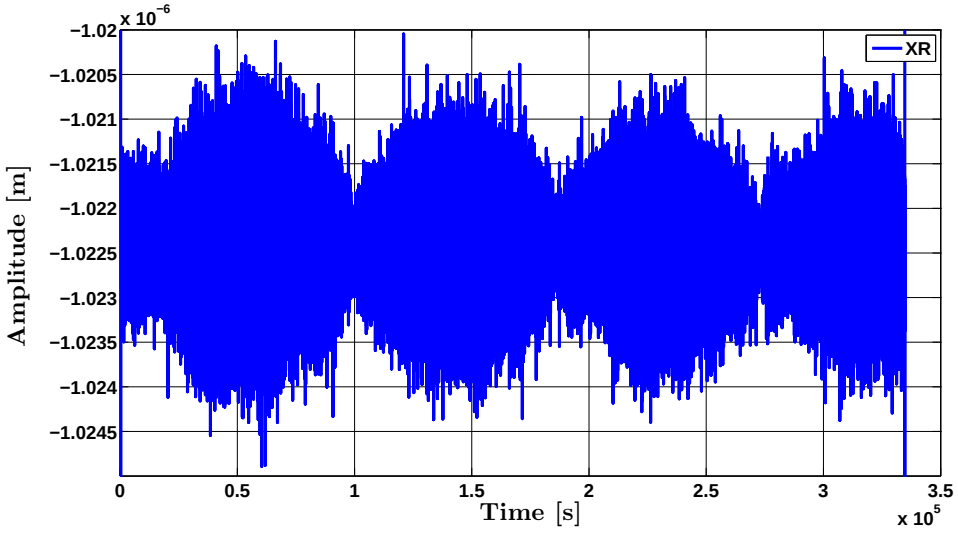

Figure 4.9.: This plot shows the phasemeter output of X_R for the measurement in Figure 4.8, it shows a dependence of the fluctuations on day and night.

4.10. Measurements with moving test masses are dominated by driver and piezo noise, so that possible side effects of the housing could not be seen. A digital setup for TM motion is planned, similar measurements will be performed in the future, if the the actuator noise can be sufficiently suppressed.
Additional to a noise investigation with motion of TM2 with housing another interesting experiment should be performed. Measurements of the impact on reflections on the inside of the housing and in the hole can be achieved with the following setup:

- A housing mockup on TM1,
- No housing mockup on TM2,
- motion of TM1.

This will be performed once the driver noise drops by to a reasonable level.

Laser frequency drift
The noise plots over different phase relations of measurement and reference beam in Chapter 3.4.3 were performed with a housing mockup on TM2, and no mockup on TM1.
A difference between the noise shapes of X_1 and X_{12} can be seen in the measurements with a generally lower noise level. Phase noise has a bigger impact on the performance than amplitude noise; measurements with high phase noise show little to no difference between the interferometers.
In the measurement with only amplitude noise the X12 noise curve is above X_1 (Figure 3.17). It is important to note that the performance and contrast of the X_{12} interferometer were always worse than X_1. The impact of the housing mockup is hard to separate from this.

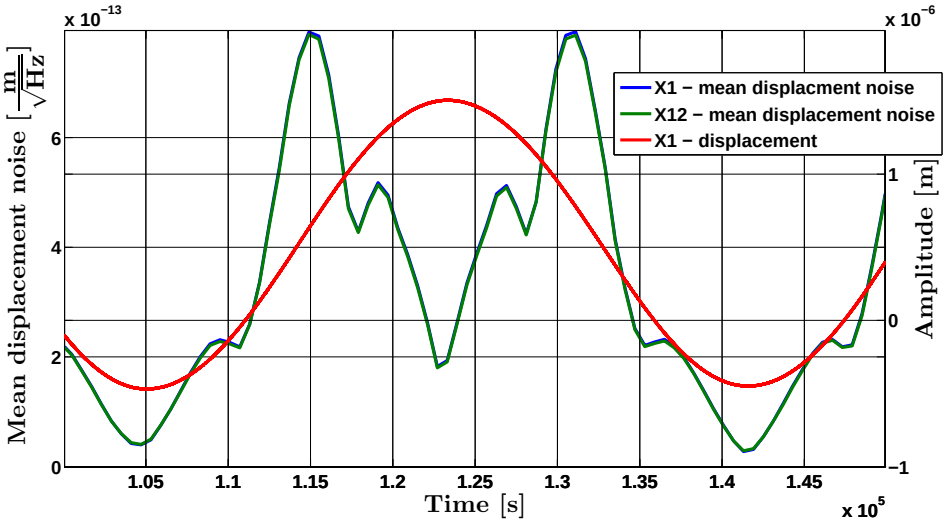

Figure 4.10.: Only TM2 is equipped with the housing mockup, TM1 is moved with a high voltage input. The displacement is shown in the red curve and Y-axis on the right side. The Y-axis on the left side shows the mean displacement noise level, it can be seen that the noise behaviour of X_1 (blue) and X_{12} (green) is very similar for big test mass movements and beam jitter. The plot shows an extract of Figure 3.12.

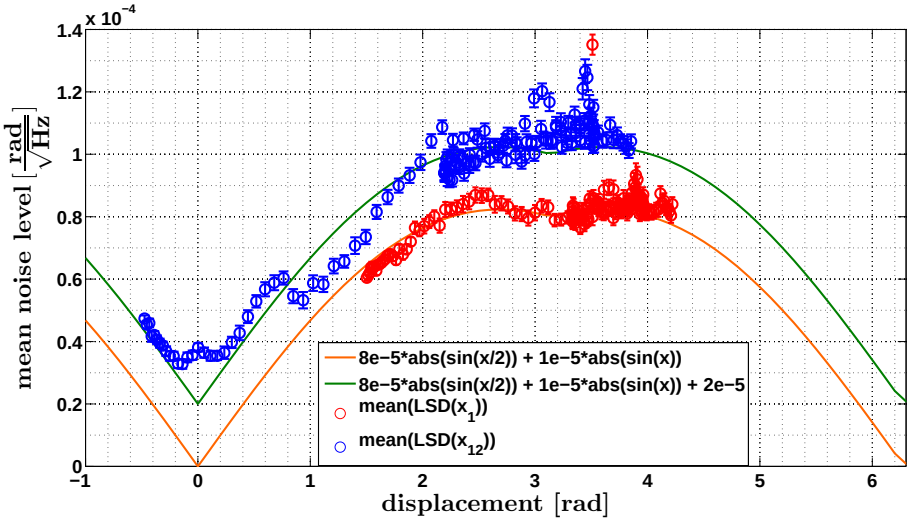

Figure 4.11.: This was shown in Chapter 3.4.3. Laser frequency drift is used to scan the noise shape for different phase relations, no test mass is moved. The X_{12} interferometer noise is higher than of the X_1 interferometers. This measurement features both amplitude and phase noise.

4.3.2. Angular motion

Motion measurements with both housings were performed. Angular movement of TM1 in ϕ and η of $1.5 \cdot 10^{-5}$ rad only lead to minor noise level changes.

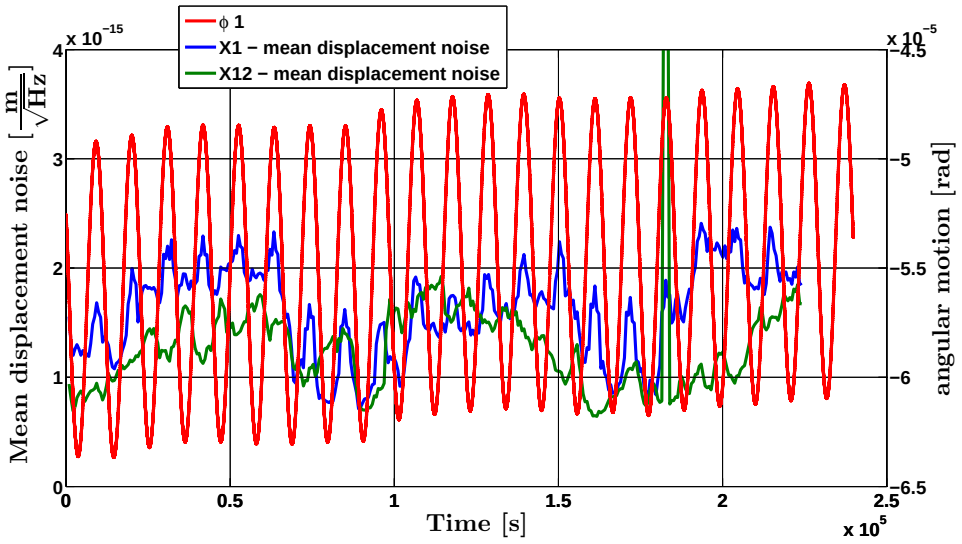

Figure 4.12.: Both test masses are equipped with a housing, the test mass is moved in ϕ. The mean displacement noise depends either on the angular motion or residual longitudinal motion.

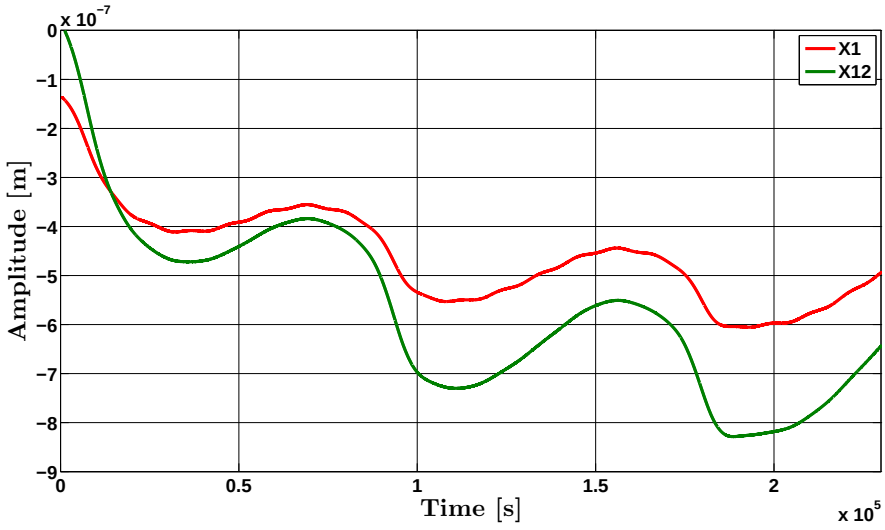

Figure 4.13.: This is the time longitudinal motion of the measurement from Figure 4.12, the small fluctuations have the same frequency as the angular motion.

5 Summary and Outlook

The subject of this thesis is the LISA Pathfinder OMS ground setup. The core components are two moveable mirrors and four interferometers. The mirrors replace the free falling test masses of the LISA Pathfinder flight model. The interferometers are bonded on an optical bench, with the X_1 interferometer the displacement fluctuations between test mass mirror 1 and the optical bench are measured. The displacement fluctuations between test mass 1 and 2 are measured with the X_{12} interferometer.
Laser Amplitude noise is measured with one additional photodiode per laser beam; this signal is used in the amplitude loop to suppress this noise. The laser frequency noise is measured with an additional interferometer and another control loop uses this signal to suppress frequency noise. Phase noise is measured with the reference interferometer and fluctuations between the two laser beams are suppressed with the OPD loop. Amplitude and Phase noise common to all interferometers is suppressed by subtracting the reference interferometer signal from the other signals, according to:

$$\begin{aligned}
\Phi_{\mathrm{R}}[\mathrm{m}] &= \frac{4\pi}{\lambda}\phi_{\mathrm{R}}[\mathrm{rad}], \\
\Phi_{\mathrm{X1}}[\mathrm{m}] &= \frac{4\pi}{\lambda}(\phi_{\mathrm{X1}}[\mathrm{rad}] - \phi_{\mathrm{R}}[\mathrm{rad}]), \\
\Phi_{\mathrm{X12}}[\mathrm{m}] &= \frac{4\pi}{\lambda}(\phi_{\mathrm{X12}}[\mathrm{rad}] - \phi_{\mathrm{R}}[\mathrm{rad}]).
\end{aligned}$$

Predictions made by Hechenblaikner [18] show that the efficiency of this subtraction depends on the phase difference, $\Delta\phi$, between the signals. The mean displacement noise level for shorter time segments of the long-term measurement was calculated. Investigations of this noise level over time and at different TM positions were done. The measurements showed the predicted $\sin^2(\phi)$ behaviour for phase noise, and an amplitude noise dependence of $\sin^2(\frac{\phi}{2})$ on the phase difference $\Delta\phi$ between the signals.
Pphase noise from sidebands originating from electrical crosstalk between the AOMs is not taken into account in this analysis [4][9][13]. In addition doppler effects in the phasemeter were not included in the analysis. In the future the analysis should be

improved to subtract these two effects.
Since excess noise from the actuator dominates this effect, the measurements were performed by changing the laser frequency, thus leading to a phase difference between measurement and reference beam.

The flight model features an electrode housing around the test masses such that on the way to the test mass the laser beam travels through a hole. This housing is missing in the ground setup. A housing mockup was designed to imitate the effect of the hole and reflective surface. Measurements showed slight negative effects on the performance of the X_{12} interferometer, but more experiments should be done to make sure that this is repeatable. It may have simply been due to bad alignment or positioning of the housing.

Currently the control loops and TM motion are realised with an analog setup. A transfer to a digital setup is planned, giving the advantage that the setup can be monitored more closely and can be changed easier.
Loop gain fluctuations and piezo input voltage can be plotted together with the interferometer signals, and adjusted on the fly if necessary.
The input voltage to the frequency and amplitude control loops drifts significantly, part of the noise change is probably due to different efficiencies of the control loops. Before every measurement the input voltage was re-adjusted, an experience based estimate of the most likely drift direction and size was not always successful.
It should be possible to generate improved drive signals for the piezos using the high quality digital outputs of the new system. Another digital control loop is planned where the test mass mirrors will be moved to counter the thermal drift and perform stable measurements over several weeks, assuming the actuator noise can be sufficiently suppressed.
Noise measurements with test mass motion will be done again, and it will be interesting to measure the path length dependant noise subtraction efficiency at different test mass positions instead of the work-around with different laser frequencies. It is expected that the effect of motion on the noise performance with housing mockups will show clearer results. The number of experiments to determine properties of the housing were limited since these take a long time to perform. It is necessary to open the vacuum tank for every change and to pump it down again.
The noise dependence was calculated only in the frequency band between 0.1 Hz and 1 Hz, the same should be done for more bands and a broader range of interferometer setups. This will be part of a paper that is currently in progress.

A Appendix

A.1. Matlab code for noise investigation

This code was written in cooperation with Nikos Karnesis during his stay at the AEI.

```
clear all;
clc;

%addpath('/my/path/here/scripts_Andi')
%addpath('/my/other/path/here/helper')
addpath('/home/anwitt/Documents/MATLAB/scripts/helper');

% define folders and measurement
% this assumes that the general evaluation was already done
datadir  = '2013-09-06_15-52';

%pRoot = fullfile(filesep, 'another', 'path', 'here', 'to', 'data');

% make figures direction
mkdir(fullfile(pRoot, datadir, 'figures', 'split'));

% go to data direction
p      = fullfile(pRoot, datadir, 'figures', 'split');
cd(pRoot);

%% load data
 D = ao.load(fullfile(pRoot, datadir, sprintf('data.mat')));

%% Extract the objects from the data and split them

% first interpolation from 32.4... to 32
Drs = fixfs(D, plist('fs', 32));
save(Drs, sprintf('%s/data_resample_32.mat', datadir));
clear D;

X         = omsCalibrateLong(Drs);
X_1_full  = X.getObjectAtIndex(1);
X_12_full = X.getObjectAtIndex(2);
X_R_full  = X.getObjectAtIndex(3);
```

```
35 X_F_full  = X.getObjectAtIndex(4);
36
37 % Split last and first disturbed segments
38 spl = plist('offsets', [1e3 -1e3]);
39
40 X_1_full  = split(X_1_full, spl);
41 X_12_full = split(X_12_full, spl);
42 X_R_full  = split(X_R_full, spl);
43 X_F_full  = split(X_F_full, spl);
44
45 % Bandpass and plot
46
47 fs   = X_1_full.fs;
48 bppl = plist('type','bandpass','fs', fs,'fc',[0.003 0.03],'order',2);
49 bp   = miir( bppl );
50 fpl = plist(param('filter', bp));
51
52 % filter
53 x1_f  = filtfilt( X_1_full, fpl);
54 x12_f = filtfilt( X_12_full, fpl);
55
56 % declare constant
57 const = ao(4*pi/1064.e-9);
58 const.setYunits('[rad][m^-1]');
59
60 iplot(const*X_1_full, const*X_12_full)
61
62 pl2 = plist('arrangement', 'subplots');
63
64 iplot(x1_f,  sin(const*X_1_full),  pl2)
65 saveas(gcf, sprintf('%s/X1_bandpassed_TS.eps',p), 'psc2')
66 saveas(gcf, sprintf('%s/X1_bandpassed_TS.fig',p))
67
68 iplot(x12_f, sin(const*X_12_full), pl2)
69 saveas(gcf, sprintf('%s/X12_bandpassed_TS.eps',p), 'psc2')
70 saveas(gcf, sprintf('%s/X12_bandpassed_TS.fig',p))
71
72 %% Split in times
73
74 % number of segments
75 segs = 94;
76
77 %time overlap
78 ovLap = 1800;
79 times = zeros(1, segs);
80
81 % create times vector
82 for ii = 1:segs
83
84   times(2*ii-1) = ii*2000+50000;
85   times(2*ii) = ii*2000+ovLap+50000;
86
87 end
88
89 % split the time series
90 x1_s  = split(X_1_full,  plist('times', times));
91 x12_s = split(X_12_full, plist('times', times));
```

```
92
93  % check if the split is ok
94  iplot(X_1_full, x1_s);
95
96  %% Loop to calculate the position and spectra
97
98  % plist definition
99  ppl = plist('Kdes',  50, 'order', 1, ...
100             'Jdes',  500,'win', specwin('Kaiser', 10, 70),...
101             'Scale', 'ASD');
102
103 % LPSD of all segments
104 x1_s_lsd  = lpsd(x1_s,  ppl);
105 x12_s_lsd = lpsd(x12_s, ppl);
106
107 % initialize
108 mean1    = ao.initObjectWithSize(1, length(x1_s_lsd));
109 mean12   = ao.initObjectWithSize(1, length(x1_s_lsd));
110 pos_er1  = ao.initObjectWithSize(1, length(x1_s_lsd));
111 pos_er12 = ao.initObjectWithSize(1, length(x1_s_lsd));
112
113 % Loop over the number of objects
114 for ii = 1:length(x1_s_lsd)
115
116   % find mean and standard deviation
117   pos_er1(ii)  = 4*pi*std(x1_s(ii))/1064.e-9/sqrt(numel(x1_s(ii)));
118   pos_er12(ii) = 4*pi*std(x12_s(ii))/1064.e-9/sqrt(numel(x12_s(ii)));
119
120   mean1(ii)    = 4*pi*mean(x1_s(ii))/1064.e-9;
121   mean12(ii)   = 4*pi*mean(x12_s(ii))/1064.e-9;
122
123   mean1(ii).setDy(pos_er1(ii).y);
124   mean12(ii).setDy(pos_er12(ii).y);
125
126   x1_s_lsd(ii).setDescription(...
127   sprintf('x1 start = %d stop = %d mean=%6.4g rad sin(m)=%6.2g', ...
128   times(ii), times(ii)+ovLap, mean1(ii).y, sin(mean1(ii).y)));
129
130   x12_s_lsd(ii).setDescription(...
131   sprintf('x12 start = %d stop = %d mean=%6.4g rad sin(m)=%6.2g', ...
132   times(ii), times(ii)+ovLap, mean12(ii).y, sin(mean12(ii).y)));
133
134 end
135
136 % Save them
137 save(x1_s_lsd,  sprintf('%s/x1_s_lsd', datadir));
138 save(x12_s_lsd, sprintf('%s/x12_s_lsd', datadir));
139
140 %% Do plots of the spectra
141
142 % build specs
143 x   = linspace(0.001, 0.03, 100);
144 y   = sqrt(( 1 + (x/0.003).^(-4) )) * 90e-12;%/1.064e-6*2*pi;
145
146 % mission goal
147 m_goal = ao(fsdata(x,y));
148 m_goal.setXunits('Hz');
```

```
149 m_goal.setYunits(x1_s_lsd(1).yunits);
150
151 %interferometer goal
152 i_goal = m_goal/10;
153 %each interferometer contribution
154 c_goal = i_goal/10;
155
156 len     = 2*numel(x1_s_lsd) + 3;
157 clrs    = cell(1, len);
158 clrs(:) = {''};
159 clrs(len-3:end) = {'k'};
160
161 % Do plot
162 [figall,ax1] = iplot(x1_s_lsd, x12_s_lsd, m_goal, i_goal, c_goal, ...
163                      plist('Linecolors', clrs));
164
165 legend('off');
166 legend(gca, x1_s_lsd.description, x12_s_lsd.description);
167
168 % save it
169 saveas(gcf, sprintf('%s/X1_X12_LSD_segments.eps', p), 'psc2')
170 saveas(gcf, sprintf('%s/X1_X12_LSD_segments.fig', p))
171
172 %% Select the frequency
173 x1_lsd_s  = split(x1_s_lsd,  plist('frequencies',[0.1 1]));
174 x12_lsd_s = split(x12_s_lsd, plist('frequencies',[0.1 1]));
175
176
177 %% X-Y plot with mean
178
179 x1_lsd_mean   = mean(x1_lsd_s);
180 x12_lsd_mean  = mean(x12_lsd_s);
181
182 x1y_mean      = ao(xydata(mean1.y,  x1_lsd_mean.y));
183 x12y_mean     = ao(xydata(mean12.y, x12_lsd_mean.y));
184
185 x1y_mean_rad  = x1y_mean/1064e-9*4*pi;
186 x12y_mean_rad = x12y_mean/1064e-9*4*pi;
187
188 % set errors
189 x1y_mean_rad.setDy(x1_lsd_mean.dy/1064e-9*4*pi);
190 x12y_mean_rad.setDy(x1_lsd_mean.dy/1064e-9*4*pi);
191
192 x1y_mean_rad.setDx(mean1.dy);
193 x12y_mean_rad.setDx(mean1.dy);
194
195 % set the correct units
196 x1y_mean_rad.setYunits('[rad][Hz^(-.5)]');
197 x12y_mean_rad.setYunits('[rad][Hz^(-.5)]');
198 x1y_mean_rad.setXunits('rad');
199 x12y_mean_rad.setXunits('rad');
200
201 % get sinewave
202 func = '1.8e-3*abs(sin(x))';
203
204 % ao-sinewave
205 sinewave = ao(plist('x', -50:0.1:50, 'xyfcn', func, ...
```

```
206              'Yunits', '[rad][Hz^(-.5)]', 'Xunits', 'rad'));
207
208 % plot plist
209 plotpl = plist('markers', {'','x','x'},...
210           'linestyles', {'-', 'none', 'none'}, 'Xranges', {'all', [-5 2]},...
211           'legends', { func, 'mean(LSD(x_1))', 'mean(LSD(x_{12}))'},...
212           'autoerrors', true);
213
214 % plot it
215 iplot(sinewave, x1y_mean_rad, x12y_mean_rad, plotpl)
216
217 % save it
218 saveas(gcf, sprintf('%s/amp_noise.eps', p), 'psc2')
219 saveas(gcf, sprintf('%s/amp_noise.fig', p))
220
221 %% X-Y plot with mean, with an extra sinewave
222
223 % my function
224 func1 = '1.8e-3*abs(sin(x))';
225
226 % create ao sinewave
227 sinewave1 = ao(plist('x', -50:0.1:50, 'xyfcn', func1, ...
228                      'Yunits', '[rad][Hz^(-.5)]', 'Xunits', 'rad'));
229
230 func2 = '1.3e-4*abs(sin(x/2)) + 2e-5';
231
232 sinewave2 = ao(plist('x', -50:0.1:50, 'xyfcn', func2, ...
233                      'Yunits', '[rad][Hz^(-.5)]', 'Xunits', 'rad'));
234
235 plotpl = plist('markers', {'', '', 'x','x'},'linestyles',...
236 {'-', '-', 'none', 'none'}, 'Xranges',{'all', [-10 2]},'legends',...
237 { func1, func2, 'mean(LSD(x_1))', 'mean(LSD(x_{12}))'},..
238 'autoerrors', true);
239
240 % plot
241 iplot(sinewave1, sinewave2, x1y_mean_rad, x12y_mean_rad, plotpl)
242 grid off
243 grid(gca,'minor')
244
245 % save it
246 saveas(gcf, sprintf('%s/amp_noise_xtraSin.eps', p), 'psc2')
247 saveas(gcf, sprintf('%s/amp_noise_xtraSin.fig', p))
248
249 %% X-Y plot 0-2pi range
250
251 sinewrap = split(sinewave, plist('times', [0 2*pi]));
252
253 % wrap all point from 0-2*pi
254 x1 = wrapTo2Pi(x1y_mean_rad.x);
255 x2 = wrapTo2Pi(x12y_mean_rad.x);
256
257 x1y_wrap  = ao(xydata(x1,  x1y_mean_rad.y));
258 x12y_wrap = ao(xydata(x2,  x12y_mean_rad.y));
259
260 x1y_wrap.setDy(x1_lsd_mean.dy/1064e-9*4*pi);
261 x12y_wrap.setDy(x1_lsd_mean.dy/1064e-9*4*pi);
262
```

```
263 x1y_wrap.setDx(mean1.dy);
264 x12y_wrap.setDx(mean1.dy);
265
266 plotpl = plist('markers', {'','o','o'},...
267 'linestyles', {'-', 'none', 'none'}, 'Xranges', {'all', [0 2*pi]},...
268 'legends', { func, 'mean(LSD(x_1))', 'mean(LSD(x_{12}))'},...
269 'autoerrors', true);
270
271 % Do plot
272 iplot(sinewrap, x1y_wrap, x12y_wrap, plotpl)
273 grid off
274 grid(gca,'minor')
275
276 % fix x-ticks (NEED THE FUNCTION 'my_xticklabels'. Free on
277 % MATLAB File Exchange)
278 pos = 0:pi/2:2*pi;
279 my_xticklabels(pos, {'0', '\pi/2','\pi','3\pi/2', '2\pi'});
280
281 % save it
282 saveas(gcf, sprintf('%s/amp_noise_folded.eps', p), 'psc2')
283 saveas(gcf, sprintf('%s/amp_noise_folded.fig', p))
284
285 %% X-Y plot 0-2pi range with a curve fit on the spectra
286
287 % initialize
288 N           = 1;
289 px1         = pest.initObjectWithSize(1, numel(x1_lsd_s));
290 px12        = pest.initObjectWithSize(1, numel(x1_lsd_s));
291 line_x1     = ao.initObjectWithSize(1, numel(x1_lsd_s));
292 line_x12    = ao.initObjectWithSize(1, numel(x1_lsd_s));
293 x1_line_er  = ao.initObjectWithSize(1, numel(x1_lsd_s));
294 x12_line_er = ao.initObjectWithSize(1, numel(x1_lsd_s));
295
296 % do a mean
297 x1_line_mean  = ao.initObjectWithSize(1, numel(x1_lsd_s));
298 x12_line_mean = ao.initObjectWithSize(1, numel(x1_lsd_s));
299
300 for ii = 1:numel(x1_lsd_s)
301
302   % run polyfit/fit lines
303   px1(ii)  = polyfit(x1_lsd_s(ii),  plist('N', N));
304   px12(ii) = polyfit(x12_lsd_s(ii), plist('N', N));
305
306   px1(ii).setDescription(sprintf('x1 fit, segment %d', ii));
307   px12(ii).setDescription(sprintf('x12 fit, segment %d', ii));
308
309   line_x1(ii)  = px1(ii).eval(plist('type', 'tsdata', 'XData',...
310   x1_lsd_s(ii), 'Xfield', 'x'));
311   line_x12(ii) = px12(ii).eval(plist('type', 'tsdata', 'XData',...
312   x1_lsd_s(ii), 'Xfield', 'x'));
313
314   line_x1(ii).setDescription(sprintf('x1 line fit, segment %d', ii));
315   line_x12(ii).setDescription(sprintf('x12 line fit, segment %d', ii));
316
317   x1_line_er(ii)  = std(line_x1(ii))/sqrt(numel(line_x1(ii)));
318   x12_line_er(ii) = std(line_x1(ii))/sqrt(numel(line_x1(ii)));
319
```

```
320    x1_line_mean(ii)   = mean(line_x1(ii));
321    x12_line_mean(ii) = mean(line_x12(ii));
322
323    x1_line_mean(ii).setDy(x1_line_er(ii).y);
324    x12_line_mean(ii).setDy(x12_line_er(ii).y);
325
326  end
327
328  % save
329  save(px1,  sprintf('%s/pest_x1', datadir));
330  save(px12, sprintf('%s/pest_x1', datadir));
331
332  save(line_x1,  sprintf('%s/line_x1', datadir));
333  save(line_x12, sprintf('%s/line_x1', datadir));
334
335  x1y_mean_line  = ao(xydata(mean1.y,  x1_line_mean.y));
336  x12y_mean_line = ao(xydata(mean12.y, x12_line_mean.y));
337
338  x1y_line_rad   = x1y_mean_line/1064e-9*4*pi;
339  x12y_line_rad  = x12y_mean_line/1064e-9*4*pi;
340
341  % Assign errors
342  x1y_line_rad.setDy(x1_line_er.y/1064e-9*4*pi);
343  x12y_line_rad.setDy(x1_line_er.y/1064e-9*4*pi);
344
345  x1y_line_rad.setDx(mean1.dy);
346  x12y_line_rad.setDx(mean1.dy);
347
348  % the correct units
349  x1y_line_rad.setYunits('[rad][Hz^(-.5)]');
350  x12y_line_rad.setYunits('[rad][Hz^(-.5)]');
351  x1y_line_rad.setXunits('rad');
352  x12y_line_rad.setXunits('rad');
353
354  % get sinewave
355  func = '1.8e-3*abs(sin(x))';
356
357  sinewave = ao(plist('x', -50:0.1:50, 'xyfcn', func, ...
358                      'Yunits', '[rad][Hz^(-.5)]', 'Xunits', 'rad'));
359
360  plotpl = plist('markers', {'','.','.'},...
361  'linestyles', {'-', 'none', 'none'}, 'Xranges', {'all', [-5 2]},...
362  'legends', { func, 'mean(LSD(x_1))', 'mean(LSD(x_{12}))'},...
363  'autoerrors', true);
364
365  iplot(sinewave, x1y_line_rad, x12y_line_rad, plotpl)
366
367  % save it
368  saveas(gcf, sprintf('%s/amp_noise_fitLines.eps', p), 'psc2')
369  saveas(gcf, sprintf('%s/amp_noise_fitLines.fig', p))
370
371
372  x1 = wrapTo2Pi(x1y_line_rad.x);
373  x2 = wrapTo2Pi(x12y_line_rad.x);
374
375  x1y_wrap_line  = ao(xydata(x1,  x1y_line_rad.y));
376  x12y_wrap_line = ao(xydata(x2,  x12y_line_rad.y));
```

```
377
378 x1y_wrap_line.setDy(x1y_line_rad.dy);
379 x12y_wrap_line.setDy(x1y_line_rad.dy);
380
381 x1y_wrap_line.setDx(mean1.dy);
382 x12y_wrap_line.setDx(mean1.dy);
383
384 iplot(sinewrap, x1y_wrap_line, x12y_wrap_line,
385 plist('markers', {'','.','.'},'linestyles', {'-', 'none', 'none'},..
386 'Xranges', {'all', [0 2*pi]},'legends', { func, 'mean(LSD(x_1))',..
387 'mean(LSD(x_{12}))'}, 'autoerrors', true))
388
389 % save it
390 saveas(gcf, sprintf('%s/amp_noise_folded_fitLines.eps', p), 'psc2')
391 saveas(gcf, sprintf('%s/amp_noise_folded_fitLines.fig', p))
```

Bibliography

[1] Albert Einstein. Prinzipielles zur allgemeinen relativitätstheorie. *Annalen der Physik*, 55:4, 1918. 1

[2] Press release: The 1993 nobel prize in physics. *Nobel Media AB*, 2013. 1

[3] Karsten Danzmann, Albrecht Rüdiger, Roland Schilling, Walter Winkler, J. Hough, P. L. Bender, and C. D. Edwards. Lisa (laser interferometer space antenna). proposal for a laser-interferometric gravitational wave detector in space. *MPQ-Reports*, 177(ID: 372299.0):192, 1993. 1

[4] Felipe Guzmán Cervantes. *Gravitational wave observation from space: optical phase measurments for LISA and LISA Pathfinder*. PhD thesis, Max Planck Institute for Gravitational Physics (Albert-Einstein-Institute), 2009. 2, 5, 7, 8, 53

[5] V. Wand F. Steier F.Guzmán A. Garciaa, G. Heinzel. Performance analysis of the fast ltp interferometric control loops: Opd and laser frequency s2-aei-tn-3035. Technical report, AEI Hannover, 2009. 2, 13, 16

[6] Frank Steier. *Interferometry techniques for spaceborne gravitational wave detectors*. PhD thesis, Laser Interferometry & Gravitational Wave Astronomy, AEI-Hannover, MPI for Gravitational Physics, Max Planck Society, escidoc:24010, 2008. 2, 5

[7] Sheila Rowan Matthew Pitkin, Stuart Reid and Jim Hough. Gravitational wave detection by interferometry (ground and space). *Living Rev. Relativity Online Article, http://www.livingreviews.org/lrr-2011-5*, 14:75, 2011. 2

[8] Vinzenz Wand. *Interferometry at low frequencies: Optical phase measurment for LISA and LISA Pathfinder*. PhD thesis, Leibniz Universität Hannover, 2007. 5, 7

[9] Anneke Monsky. *Understanding interferometric drag-free sensors in space using intelligent data analysis tools*. PhD thesis, Max Planck Institute for Gravitational Physics (Albert-Einstein-Institute), 2010. 5, 53

[10] Gerhard Heinzel, Frank Steier, Roland Fleddermann, Benjamin Sheard, and Karsten Danzmann. Components for the lisa local interferometry. In *LASER*

INTERFEROMETER SPACE ANTENNA: 6th International LISA Symposium Veranstaltungsort Greenbelt, Maryland, volume 873, 2006. 5

[11] Gerhard Heinzel. *Advanced optical techniques for laser-interferometric gravitational-wave detectors*. PhD thesis, Max Planck Institute for Gravitational Physics (Albert-Einstein-Institute), 1999. 7, 8

[12] D. J. McCarron. A guide to acousta-optic modulators, 2007. 9

[13] A. García F. Guzmán F. Steier C. Killow D. Robertson H. Ward C. Braxmaier G. Heinzel, V. Wand. Investigation of noise sources in the ltp interferometer s2-aei-tn-3028 2005/10/20. Technical report, AEI Hannover, University of Glasgow, EADS Astrium Immenstaad, 2005. 10, 12, 13, 16, 40, 41, 42, 53

[14] Antonio Garcia Martin Hewitson. Laser amplitude noise characterisation for ltp s2-aei-tn-3055. Technical report, Max Planck Institute for Gravitational Physics (Albert-Einstein-Institute) Università degli studi di trento, January 15, 2009. 12

[15] *Mephisto Product Line - User's Manual*. Innolight. 12, 16

[16] Gerhard Heinzel Vinzenz Wand. Required opd precision in the ltp interferometer s2-aei-tn-3031. Technical report, Max Planck Institute for Gravitational Physics (Albert-Einstein-Institute), 2006. 13

[17] Gerhard Heinzel Antonio Garcia, Frank Steier. S2-aei-tn-30xx coupling of laser amplitude noise into the ltp phase readout noise aei internal tn. not for external distribution. Technical report, Max Planck Institute for Gravitational Physics (Albert-Einstein-Institute), 2009. 14, 25, 27, 40

[18] Gerald Hechenblaikner. Common mode noise rejection properties of amplitude and phase noise in a heterodyne interferometer. *J. Opt. Soc. Am. A 30*, 1:8, 2013. 14, 19, 27, 53

[19] Christian Killow Ewan Fitzsimons. Calculation of test mass reflection points with no optical windows s2-ugl-tn-3037. Technical report, LTP Project Institute for Gravitational Research Department of Physics and Astronomy University of Glasgow Glasgow G12 8QQ, Scotland, 2009. 42

[20] Astrium. Smart-2 optics bench mechanical interface drawing i-ke-0159-100-c. Technical report, Astrium, 2003. 42, 43

[21] Astrium. H-sideplate 1 i-ke-0159-611-b. Technical report, Astrium, 2003. 43

[22] Astrium Friedrichshaven. Dummy mirror end plate 2569 - 900 000a04b. Technical report, Astrium Friedrichshaven, 2008. 43

[23] Thales Alenia Space italia S.p.A. Lisa electrode housing interface control drawing icd750800241. Technical report, Thales Alenia Space italia S.p.A., 2009. 44

Danksagung

Die Messung von Gravitationswellen ist ein ehrgeiziges Unterfangen, so es ist es nicht verwunderlich dass viele Menschen im Lauf der Zeit an diesem Ziel gearbeitet haben. Das Ziel der LISA Mission ist die Messung von Gravitationswellen durch Laser Interferometrie im Weltraum, zur Technologie Demonstration ist die LISA Pathfinder Mission konzipiert. Mein Dank gilt allen die vor mir an diesen beiden Projekten gearbeitet haben und arbeiten und es so möglich machen dass junge Physikstudenten die Möglichkeit haben Teil von etwas etwas Großem zu sein. Insbesondere gilt mein Dank Prof. Dr. Karsten Danzmann und Dr. Gerhard Heinzel die dies in Hannover am Albert-Einstein-Institut möglich machen.
Außerdem danke ich Dr. Martin Hewitson und Heather Audley dass sie mich so nett in die LISA Pathfinder Gruppe aufgenommen haben, und mir bei vielen Problemen zur Seite standen. Zusätzliche software-seitige Unterstützung hatte ich von Ingo Diepholz und Nikos Karnesis, bei Hardware Problemen waren Andreas Weidner und Philipp Kormann vom Elektronik Workshop und Philipp Schauzu vom Mechanik Workshop eine große Hilfe.
Außerdem danke ich meinem Mitbewohner Christoph Stahl dass er nur mürrisch guckt wenn mal etwas mehr Abwasch liegen blieb während der letzten Züge dieser Masterarbeit.

Eigenständigkeitserklärung

Hiermit versichere ich, die vorliegende Arbeit selbstständig verfasst und keine anderen als die angegebenen Quellen und Hilfsmittel benutzt sowie die Zitate deutlich kenntlich gemacht zu haben.

Hannover, November 12, 2013 Andreas Wittchen